令 和 五 年 度　　修 士 論 文

Online Diagnosis of Heater Wire Breakage in Temperature Control System

指導教員　　橋本　誠司　教授

群馬大学大学院理工学府 理工学専攻
電子情報・数理教育プログラム

王　之非

Online Diagnosis of Heater Wire Breakage in Temperature Control System

Zhifei Wang

Advised by Seiji Hashimoto

Submitted to the Graduate School
of Science and Technology
at the Gunma University

February   2024

Abstract

This study investigates the diagnosis of heater disconnection using machine learning algorithms and data clustering algorithms, comparing the merits of Euclidean distance and Mahalanobis distance in the context of heater disconnection diagnosis. Initially, a simulation model is constructed in MATLAB, and through simulation runs, relevant data (voltage, current, resistance, temperature) of the heater is collected using specified settings. Subsequently, this data is utilized for learning and diagnosis by machine learning models.

Throughout the research process, various parameters are modified, and random external disturbances (perturbations) are introduced to assess the stability and accuracy of the machine learning system. Additionally, factors influencing changes in Mahalanobis distance are studied, and the predicted factors are experimentally validated.

Contents

Acknowledgements

Chapter 1

Introduction

Temperature control systems play a crucial role in various applications, ranging from industrial processes to scientific laboratories and residential environments. The ability to maintain precise and stable temperatures is essential for ensuring the efficiency and reliability of these systems. For example, temperature-control plays an important role in keeping many types of modern facilities operating efficiently, such as experimental space science instruments [1], vehicles [2], batch reactors [3], refuge chambers [4], and medicine capsuling machines [5]. However, a common challenge in temperature control systems is the occurrence of heater wire breakage, which can lead to significant operational issues. Identifying and addressing heater wire breakage promptly is paramount to prevent disruptions in production, maintain experimental integrity, and enhance the overall performance of temperature control systems.

In conventional temperature control systems, detecting heater disconnection relies on manual inspection or sensor feedback [6]. Also, The fault diagnosis methods can be typically categorised into model-based, knowledge-based, and signal-based schemes [7]. The model-based method utilises the observers such as Kalman filter, parity relation, model reference adaptive system (MRAS), mixed logical dynamic (MLD) model and so on [8–12], where the diagnosis procedure is performed by monitoring the residual signals between the measured outputs of the actual system and the estimated variables of the predefined model. A demerit of these schemes is that the diagnosis performance heavily depends on the accuracy of model parameters. Manual inspections are time-consuming and prone to human error, and subtle breaks may not be detected [13]. On the other hand, sensor-based feedback systems may be limited by the accuracy of the sensors and may not provide real-time insights into the health of the heating element. Therefore, advanced and automated diagnostic methods are necessary to overcome these limitations and improve the reliability of temperature control systems.

Integrating artificial intelligence (AI) into temperature control systems has become a promising solution to improve diagnostic capabilities. Fault diagnosis methods based on artificial intelligence usually do not require the establishment of precise mathematical models for the studied objects. According to the presence or absence of supervision, these methods can be categorized into supervised learning, semi-supervised learning, and unsupervised learning [14]. The main supervised learning methods include Artificial Neural Network (ANN) [15, 16], Support Vector Machine (SVM) [17, 18], Random Forests (RFs) [19, 20], K-Nearest Neighbor (KNN), etc.; Semi-supervised learning methods include generative methods [21] and divergence-based methods. Unsupervised learning methods mainly include Self-Organizing Maps (SOM) [22], clustering algorithms [23], Principal Component Analysis (PCA) [24, 25], etc. There are also fault diagnosis algorithms based on deep learning, reinforcement learning, and transfer learning algorithms. Methods based on deep learning include convolutional neural networks (CNN) [26, 27], deep belief networks (DBN) [28], and stacked autoencoders (SAE) [29, 30]. Methods based on reinforcement learning include Q-learning [31], and methods based on transfer learning include TrAdaBoost [32].

This paper utilizes a one-dimensional convolutional neural network (1D-CNN) model from deep learning. In the simulation model constructed in MATLAB, it learns and analyzes normal and abnormal (i.e., wire breakage) data from the heater, diagnosing heater disconnections. Additionally, considering the scarcity of abnormal situations in actual production processes (i.e., limited abnormal data), unsupervised learning techniques such as clustering algorithms (Euclidean distance and Mahalanobis distance) are employed for diagnosis of wire breakage.

This paper begins by introducing the design and construction of the simulation model, followed by an analysis of the simulation results. Next, the one-dimensional convolutional neural network (1D-CNN) model used is presented, showcasing the learning and validation results obtained from applying the 1D-CNN to the data collected from the simulation results. Subsequently, the data clustering algorithms and two distance metrics—Euclidean distance and Mahalanobis distance—are introduced. The simulation results are analyzed in terms of learning and diagnosis using these algorithms, and the paper explores two factors influencing Mahalanobis distance and their impact patterns. Finally, a summary is provided for the entire study.

Chapter 2

Temperature Control System and Simulation

2.1   Design of the Temperature Control System

The primary objective of this research is to identify instances of wire breakages, including both single and double breakages, as well as malfunctions within a system consisting of 10 parallel heaters. This detection is achieved by analyzing input parameters, namely input voltage, input current, and output temperature. The conceptual representation of the model is illustrated,

$$R_T = R_t \left[1 + \alpha_t \left(T - t \right) \right] \tag{2.1}$$

where, the resistance R_T and its corresponding temperature T are anticipated to manifest a linear functional relationship. R_T represents the resistance of the heater at a temperature T, while R_t signifies the resistance of the heater at a temperature t. α_t denotes the temperature coefficient of impedance when the temperature is t degrees Celsius.

In the context of metal conductors, it is expected that their resistance will demonstrate a distinct correlation with temperature. This relationship is a critical aspect of the proposed model, wherein the interplay between resistance and temperature serves as a pivotal indicator for detecting wire breakages and malfunctions. The comprehensive exploration of this relationship allows for a deeper understanding of the system's behavior under various conditions.   This research endeavors to advance the understanding of wire breakage detection by intricately examining the relationships between input parameters and the consequential ef-
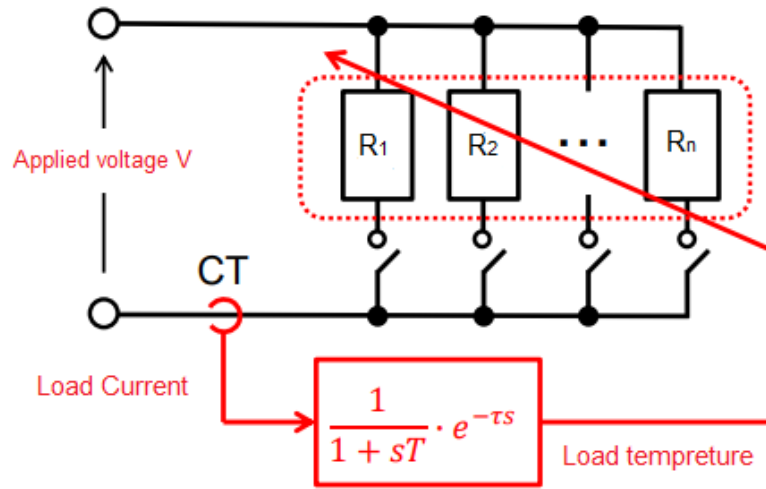
Figure 2.1: Schematic diagram of a parallel resistor wire heating system

fects on resistance and temperature. The proposed model, as depicted in Figure 2.1, represents a sophisticated framework for achieving enhanced reliability in detecting both single and double wire breakages, along with other potential malfunctions in a complex system of parallel heaters.

In the schematic diagram, applying voltage to the 10 parallel heaters results in the generation of a load current within the circuit. As a consequence, the temperature of the heaters will increase. The primary objective is to detect instances where the heaters experience wire breakages due to excessively high temperatures. Here, the relationship between the impedance and temperature of a copper wire is illustrated in Figure 2.2.

2.2   Establishment of Simulation Model

2.2.1   Simulation model for subsystem

In the practical execution of data collection and diagnostic procedures, relying solely on mathematical expressions proves inadequate for conducting meaningful simulation runs. Consequently, after abstracting the tangible quantitative relationships from the expression presented in Equation 2.1, the establishment of a robust and practical simulation model becomes imperative. This endeavor involves leveraging Simulink to create a comprehensive and intuitive simulation model, as
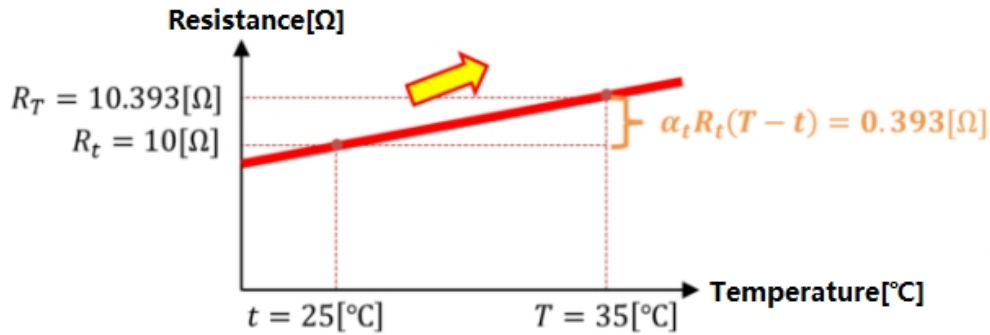
Figure 2.2: The Linear Relationship Between the Impedance and Temperature of a Copper Wire
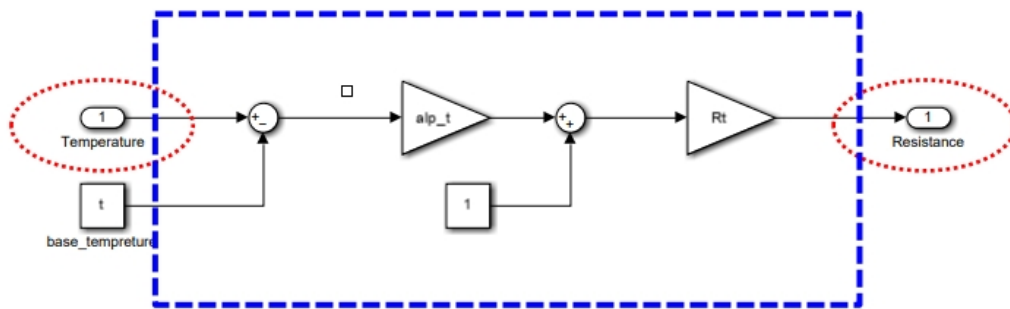
Figure 2.3: Simulation model of the impedance-temperature expression

illustrated in the accompanying figure, where, the gain, alp_t, corresponds to the temperature coefficient of impedance, α_t.

Furthermore, this simulation model is designed to function as a cohesive sub-system, seamlessly embedded within a more extensive and higher-level simulation framework. This hierarchical integration allows for a modular and scalable approach, fostering adaptability and ease of further model expansion. The utilization of Simulink, as showcased in the graphical representation, not only enhances the clarity of the simulation model but also paves the way for more advanced analyses within the broader context of the overall system simulation.

Next, it is necessary to model the schematic diagram within the dashed lines in Figure 2.1. Initially, the connection involves multiple heaters arranged in parallel. Subsequently, temperature input signals are provided, and through the subsystem depicted in Figure 2.3, corresponding resistance values are obtained. As it is a

configuration of parallel resistances, the reciprocals of individual resistance values are calculated, summed, and then reciprocated again to derive the parallel impedance, R.

Following this, based on the input voltage signal, V, and the calculated parallel impedance, R, computations yield the circuit's load current, I. It is important to note that this configuration involves parallel connections of multiple resistances, necessitating the reciprocal calculation and summation for obtaining the parallel impedance, R. Subsequently, reciprocal transformation is applied once more to finalize the impedance calculation. The illustration in Figure 2.4. depicts an example of two heaters connected in parallel.
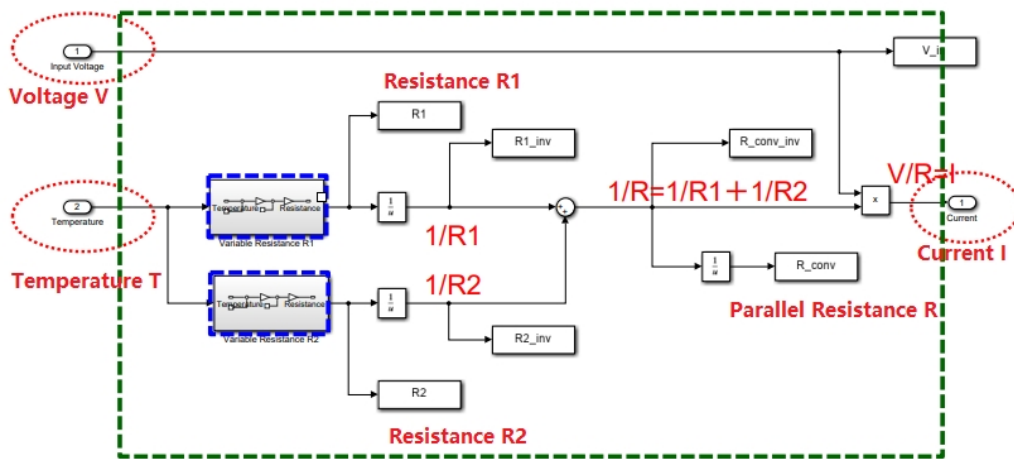
Figure 2.4: Example of two heaters connected in parallel

2.2.2 Establishment of closed-loop control model and Simulation

In practical experiments, this paper initially considers the scenario of four heaters connected in parallel. The above example is extended to incorporate four heaters in parallel, followed by the establishment of a closed-loop control model, as depicted in Figure 2.6, where, the subsystem with four heaters in parallel is encapsulated within the delineated green dashed box, constituting a comprehensive simulation model, and the magnified view of this is shown in Figure 2.5. The initiation of this model involves introducing an input temperature reference signal. Subsequently, a feedback loop is established, incorporating the negative feedback
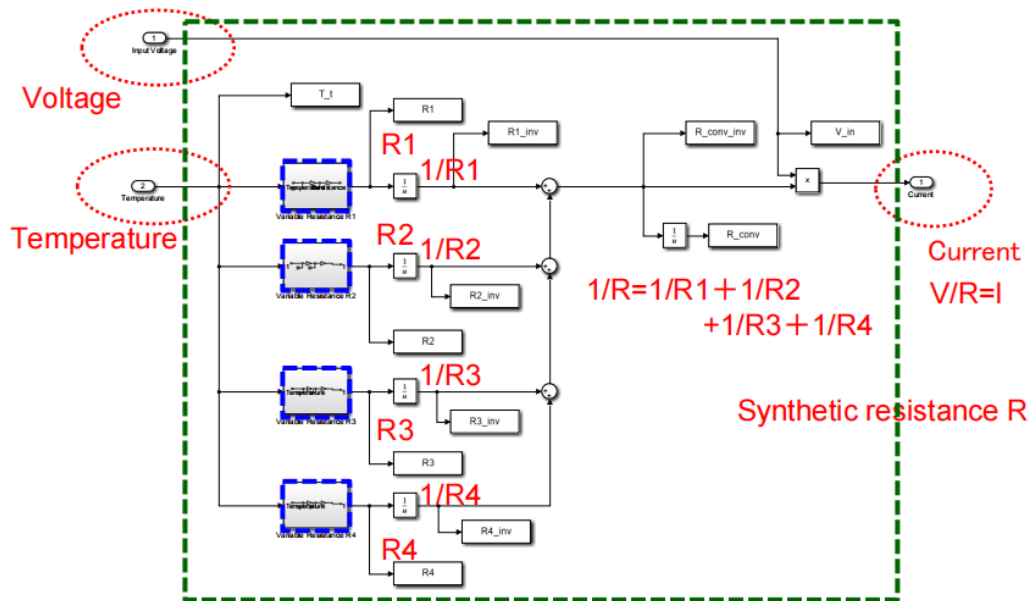
Figure 2.5: Subsystem of 4 parallel heaters

from the output temperature. The intricate dynamics within this subsystem are orchestrated through a temperature controller, yielding a voltage signal that serves as the input voltage signal for this particular module. Likewise, the negative feedback loop from the ultimate output temperature concurrently functions as the input temperature signal for this subsystem. Given that the temperature of the heaters doesn't undergo immediate discernible changes upon the generation of the load current, a deliberate delay time is incorporated. This deliberate delay is strategically imposed to facilitate a more precise and distinct observation of the heaters' temperature variations during this specified time interval.

This nuanced configuration ensures a meticulous examination of the interplay between the input temperature reference, the feedback loop, and the resulting voltage and temperature signals within the subsystem. The deliberate inclusion of a time delay feature amplifies the model's fidelity, enabling a thorough capture of the gradual temperature shifts in the heaters subsequent to the initiation of the load current.

Based on this, the simulation parameters are configured. Firstly, for the temperature controller, the sampling time is set to 0.1 seconds. Secondly, a first-order lag for the current is established with a delay time of 100 seconds, and a time delay of 5 seconds. The target output temperature value is set at 50°C, with an initial value of 0. The impedance-temperature relationship for each copper wire is

8
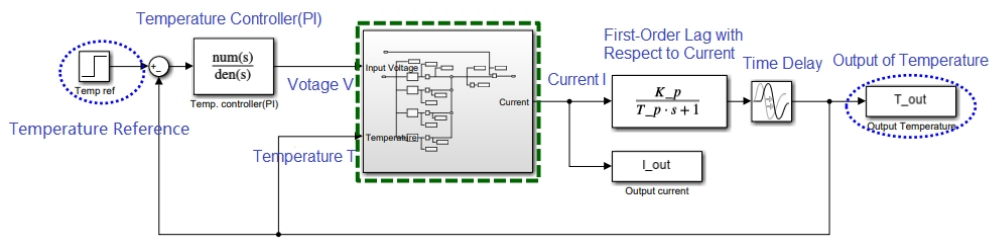
Figure 2.6: Temperature closed-loop control model
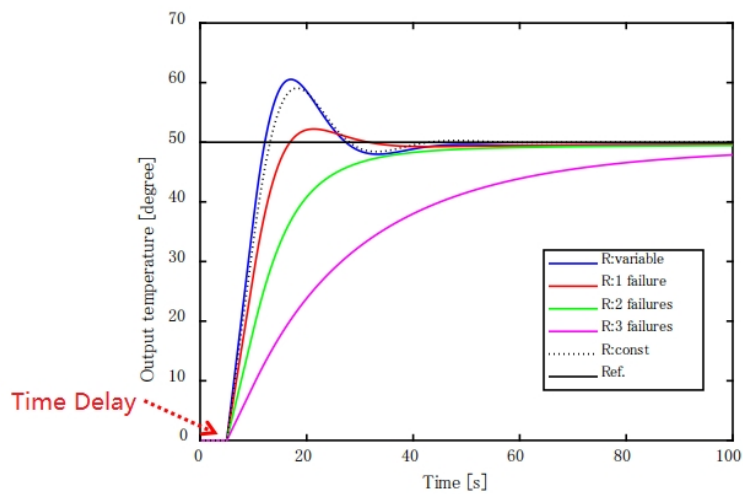
Figure 2.7: Temperature output curves for different numbers of heater wire breakages

defined as follows: at 25°C, the impedance is 10Ω, with a temperature coefficient of impedance set at 0.00393.

With these specified parameters, the simulation is executed. Assuming different numbers of heaters experiencing wire breakage (4, 3, 2, and 1), the temperature input profiles are obtained, as depicted in Figure 2.7. And the output images for input voltage versus load current are shown in Figure 2.8. The resistance value output image is presented in Figure 2.9.

2.2.3   Analysis of Initial Simulation Results

In the three aforementioned figures, the visual representation distinguishes different scenarios: the blue line signifies the normal condition, the red line rep-
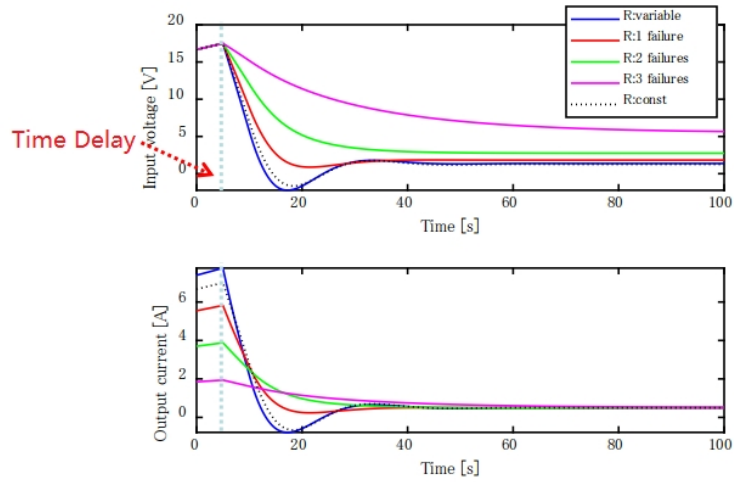
Figure 2.8: Output curves of input voltage vs. load current
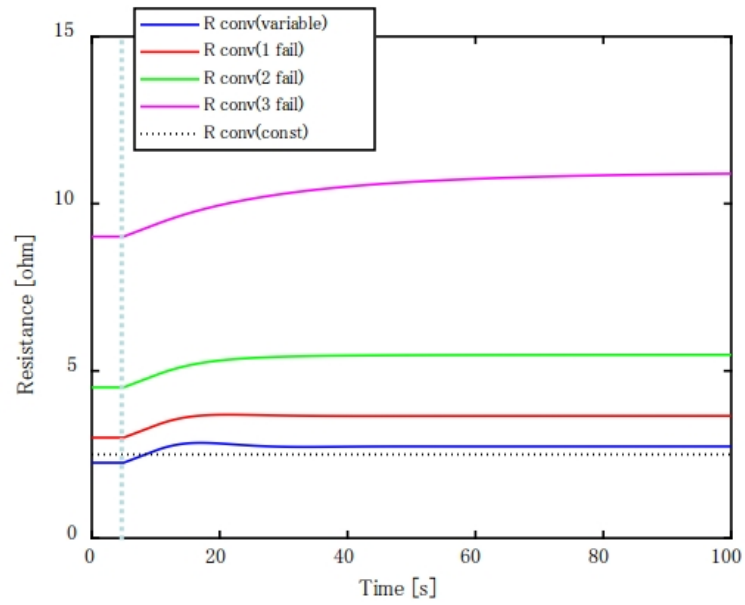
Figure 2.9: Output of resistance

resents one heater under wire breakage, the green line corresponds to two heaters under wire breakage, and the purple line indicates three heaters under wire breakage. In Figure 2.7, a discernible pattern emerges as the number of heaters experiencing wire breakage increases. Notably, the peak value of the output temperature gradually diminishes, while the response time progressively extends. This observation provides valuable insights into the impact of heater wire breakages on the dynamic behavior of the system.

Moving on to Figure 2.8, the plot unveils a nuanced relationship between input voltage and load current under varying conditions denpending on the wire breakage. As the input voltage undergoes gradual increments, an intriguing interplay unfolds. The response time exhibits an analogous lengthening, accompanied by a diminishing amplitude of oscillations. Simultaneously, the load current values experience a gradual reduction in oscillation amplitude, coupled with a steady increase in response time. This comprehensive analysis underscores a key trend: with an escalating number of heater wire breakages, the ratio of voltage to current undergoes a gradual increment, reflecting a continuous rise in impedance.

To further validate this trend, the resistance variation curve in Figure 2.9 serves as a crucial piece of evidence. The resistance variations distinctly align with the observed changes in the temperature, voltage, and current dynamics. This convergence of evidence strengthens the assertion that an increasing number of heater wire breakages correlates with a growing impedance in the system.

In summary, the detailed examination of Figures 2.7, 2.8, and 2.9 provides a comprehensive understanding of the system's response to varying degrees of heater wire breakages. These findings contribute to the broader exploration of impedance dynamics in parallel heater systems and lay the foundation for informed decision-making in the context of machine learning diagnostics.

Chapter 3

Diagnosis of Heater Wire Breakage Based on 1-D Convolutional Neural Network(1D-CNN)

Building upon the simulation model established in Chapter 2 and the initial simulation run results and analysis, the next step involves multiple iterations of the model. In each iteration, data will be collected to ensure a sufficient dataset for subsequent machine learning analysis.

3.1   1-D Convolutional Neural Network

1D-CNN refers to one-dimensional convolutional neural network (1D Convolutional Neural Network), which is a variant of convolutional neural network. 1D-CNN is mainly used to process one-dimensional sequence data, such as audio, text, etc. Compared with traditional fully connected neural networks, 1D-CNN can better handle local relationships in sequence data, and therefore performs better in tasks such as speech recognition, natural language processing, and time series prediction.   There are many advantages to using adaptive and compact 1D CNN instead of traditional (2D) deep convolutional neural network. First, compact 1D-CNN can be efficiently trained using limited 1D signal datasets, whereas 2D deep CNN typically requires large-scale datasets, such as "big data" scale datasets, in addition to requiring 1D to 2D data conversion. Prevents the well-known "overfitting" problem. One-dimensional CNN can be directly applied to raw signals (e.g. current, voltage, vibration, etc.) without any pre- or post-processing such as feature extraction, selection, dimensionality reduction, denoising, etc. Furthermore, due to the simple and compact configuration of this adaptive 1D-CNN that only performs linear 1D convolutions (scalar multiplication and addition), real-time and low-cost hardware implementation is feasible [33].
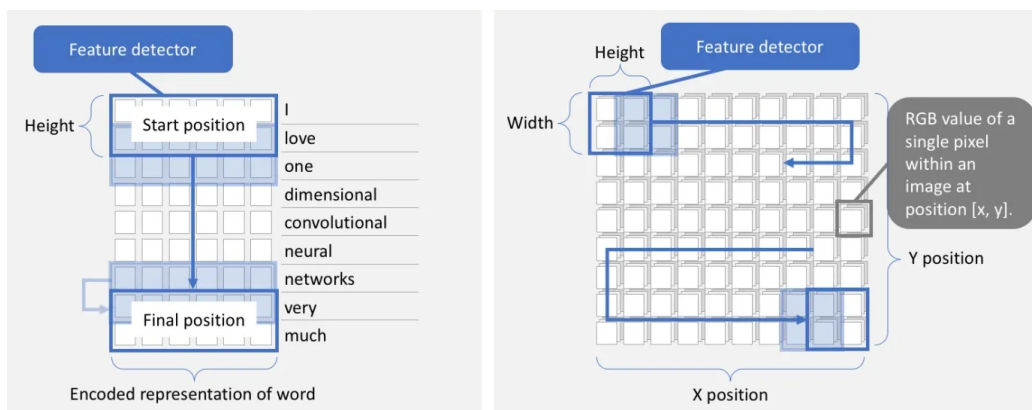
Figure 3.1: Comparison between a 1D-CNN and a 2D-CNN

The example in Figure 3.1 illustrates a simple comparison between a 1D-CNN and a 2D-CNN, in which, the left example for natural language processing, a sentence is made up of 9 words. Each word is a vector that represents a word as a low dimensional representation. The feature detector will always cover the whole word. The height determines how many words are considered when training the feature detector. In our example, the height is two. In this example the feature detector will iterate through the data 8times. In the right example for computer vision, each pixel within the image is represented by its x- and y position as well as three values (RGB). The feature detector has a dimension of 2 x 2 in our example. The feature detector will now slide both horizontally and vertically across the image.

1D-CNN usually consists of multiple alternating convolutional and pooling layers, and finally uses a fully connected layer to map the extracted features to the output. During the training process, 1D-CNN uses the backpropagation algorithm to update the model parameters to minimize the loss function.

1D-CNN mainly consists of the following parts:

Input layer: receives one-dimensional sequence data as input to the model.

Convolutional layer: uses a series of trainable convolution kernels to slide over the input data and extract features. Convolution operations can effectively extract local information and thereby capture local patterns of the input sequence.

Activation function: performs nonlinear transformation on the output of the convolution layer to enhance the expression ability of the model. Pooling layer: By reducing the dimensionality of the convolutional layer output, the amount of

calculation is reduced, while the robustness and generalization ability of the model are improved.

Fully connected layer: Maps the output of the pooling layer to the output of the model, usually used for tasks such as classification and regression.

3.2   Activation Function

In the realm of artificial neural networks, the activation function of a node plays a pivotal role in determining the node's output given a specific input or set of inputs. Analogously, envisioning a standard integrated circuit as a digital network reveals a series of activation functions, akin to being either "ON" (1) or "OFF" (0) based on the input. This analogy aligns with the concept of a linear perceptron within neural networks. However, it's crucial to note that solely nonlinear activation functions empower these networks to effectively address nontrivial problems using a minimal number of nodes. These specific activation functions, facilitating nonlinearity in computations, are aptly termed "nonlinearities."

The most prevalent activation functions are generally categorized into three groups: ridge functions, radial functions, and fold functions. An activation function, denoted as f, is considered saturating when

$$\lim_{|v| \to \infty} |\nabla f(v)| = 0 \tag{3.1}$$

Conversely, it is classified as non-saturating when it does not exhibit saturation. Non-saturating activation functions, exemplified by ReLU, may offer advantages over saturating counterparts by mitigating issues associated with gradient vanishing [34]. Ridge functions, representing the archetypal activation functions, are multivariate functions that operate on a linear combination of input variables.

Ridge functions as the most classic activation functions are multivariate functions acting on a linear combination of the input variables. Often used examples include

$$\text{Linear} \quad \text{activation} : \quad \phi(\mathbf{v}) = a + \mathbf{v}'\mathbf{b},$$

$$\text{ReLU} \quad \text{activation} : \quad \phi(\mathbf{v}) = \max(0, a + \mathbf{v}'\mathbf{b}), \tag{3.2}$$

$$\text{Logistic} \quad \text{activation} : \quad \phi(\mathbf{v}) = (1 + \exp(-a - \mathbf{v}'\mathbf{b}))^{-1}.$$

Compared with the $sigmoid$ and $Tanh$ activation functions, the ReLU function does not have the saturation problem when the input is positive, i.e., it solves the gradient vanishing problem and makes the deep network trainable; the computation velocity is very fast, and only needs to judge whether the input is greater than 0; the convergence velocity is much faster than the $sigmoid$ and $Tanh$ functions. ReLU function output will make part of the neurons to be 0, which brings network sparsity and also reduces the correlation between parameters, alleviating the problem of overfitting to a certain extent. Some activation functions are shown as follows.

$$sigmoid(x) = \frac{1}{1+e^{-x}}$$

$$tanh(x) = \frac{e^{-x}-e^{x}}{e^{-x}+e^{x}} = \frac{e^{2x}-1}{e^{2x}+1}$$

$$\text{ReLU} = \begin{cases} x, & if \quad x \geq 0 \\ 0, & if \quad x < 0 \end{cases}$$

(3.3)

3.3 Parameter Configuration and Diagnostic Results for Machine Learning and Validation

Before configuring the parameters for machine learning, considering the need for a sufficiently large dataset, it is planned to set the simulation runs to 200 times. Consequently, the target temperature input value, initially set at 50°C, will be modified to a range of 50 to 300°C. During the simulation runs, the amplitude of this input temperature signal will vary, ensuring non-repetition and integer values for each run. The simulation runtime is set at 30 seconds.

Based on this, parameters for machine learning are set. This study categorizes the detection results into three classes: normal (no heater wire breakage), abnormal 1 (one heater wire breakage), and abnormal 2 (two heater wire breakages). Within the temperature range of 91 to 100°C, with one node per 1°C, 10 step responses are obtained. The data acquisition method involves selecting data at any 2-second interval within the first 15 seconds of the response. Given a sampling time of 0.1 seconds, this results in collecting 20 sets of data for each step response. With 10 step responses, a total of 200 data points are acquired (600 sets of data in total, with 200 sets for normal data and 400 sets for abnormal 1 and abnormal 2 data combined). Among these, 80% of the data (160 sets each for normal, ab-
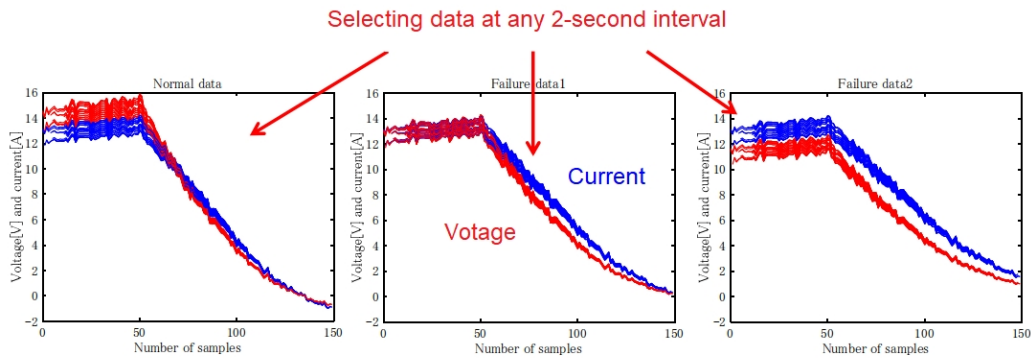
Figure 3.2: The data collected for voltage and current every second after the onset of the response at 15 seconds

normal 1 and abnormal 2) are used for learning, while the remaining 20% (40 sets each for normal, abnormal 1 and abnormal 2) are used for validation and testing. The input data consists of voltage and current.

All data after the onset of the response at 15 seconds are shown in Figure 3.2. In this figure, the red curve represents the voltage data, while the blue curve represents the current data. From left to right, the cases correspond to normal, abnormal 1, and abnormal 2 situations. It can be observed that the voltage remains relatively unchanged with an increasing number of disconnected heaters, while the current data values gradually decrease. The acquisition of data for machine learning involves randomly selecting 2-second intervals from the data starting at 15 seconds.

3.4   Analysis of Machine Learning and Validation

3.4.1   Confusion matrix

As a result, the process for machine learning is illustrated in Figure 3.3.

In machine learning, a confusion matrix is an error matrix commonly used for visually evaluating the performance of supervised learning algorithms. The confusion matrix is a square matrix of size (n_classes, n_classes), where n_classes represents the number of classes. Each row of the matrix represents instances

16

Figure 3.3: Process and results of machine learning

Figure 3.4: Single confusion matrix of 2 classes

from the true class, while each column represents instances from the predicted class (as implemented in TensorFlow and scikit-learn). Alternatively, each row can represent instances from the predicted class, and each column from the true class (as defined in the Confusion matrix from Wikipedia). Through the confusion matrix, it is easy to discern whether the system is confusing two classes, which is the origin of the name "confusion matrix."

The confusion matrix is a specific type of contingency table or cross-tabulation with two dimensions (actual and predicted) that share the same set of classes. In a contingency table, each combination of dimensions and classes represents a variable. Represented in tabular form, the contingency table visually depicts the frequency distribution of multiple variables [35]. A single confusion matrix is like what in Figure 3.4. Here, two categories for the data are established, distinguishing them into predicted values and actual values. The region shaded with light blue represents the content validated as true.
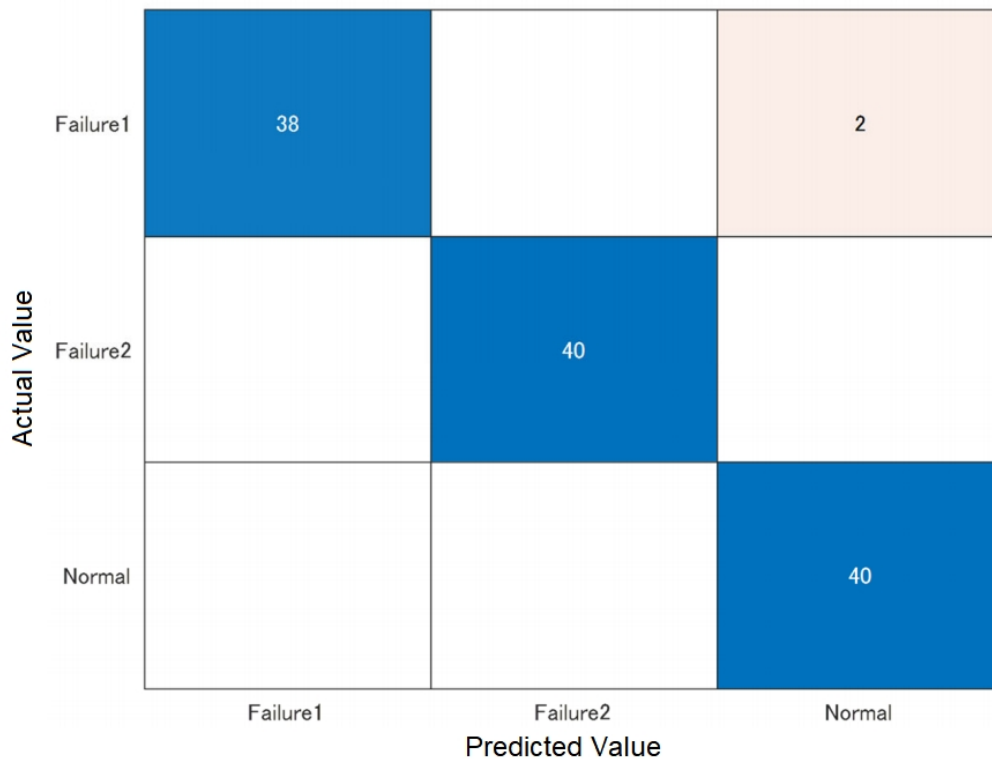
Figure 3.5: The confusion matrix depicting the validation results

Next, the results of machine learning will be presented in the form of a confusion matrix, as shown in Figure 3.5.

3.4.2 Analysis of learning results

In Figure 3.3, it is evident that during the machine learning process, a total of 4 seconds were spent on training. In the first epoch, the accuracy was only around 30%. After 15 epochs, there was a significant improvement, reaching 99.7%, close to 100%. In the actual validation results, the accuracy was 98.3%. Out of a total of 40 normal data sets and 80 abnormal data sets, there were 2 incorrect classifications.

In the confusion matrix in Figure 3.5, the blue-colored blocks represent correct classifications, while the pink-colored blocks represent incorrect classifications. Through this confusion matrix, it is evident that both types of incorrect classifications involve categorizing normal class into the abnormal 1 class.
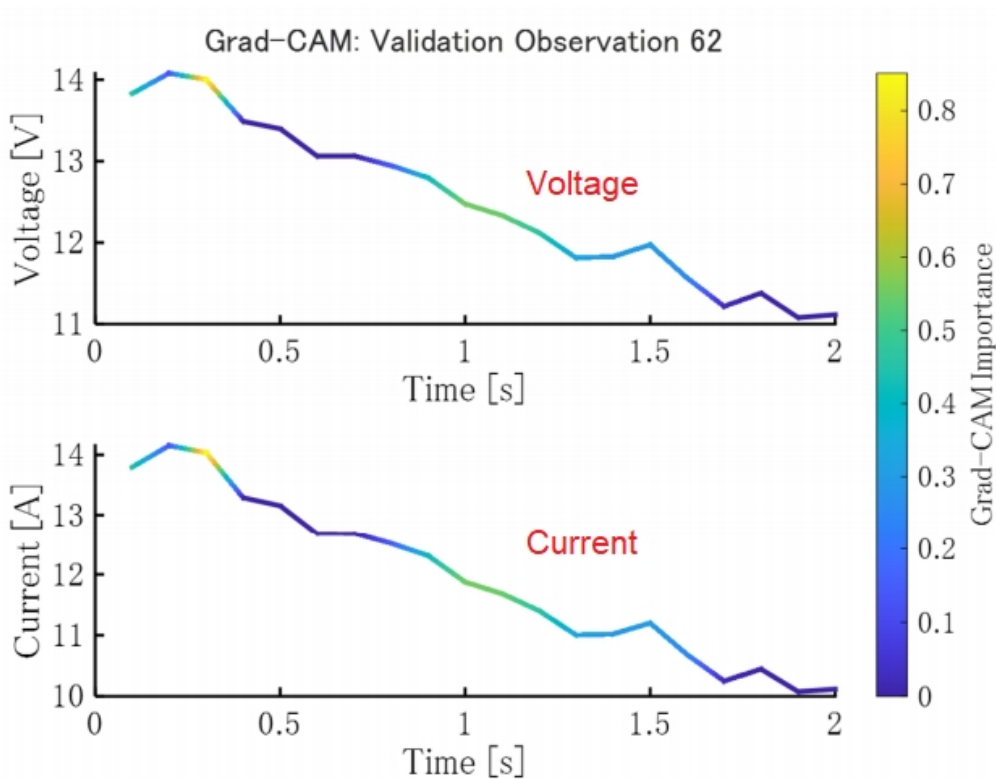
Figure 3.6: Visualization of time response (example 1)

Grad-CAM is a technique in deep learning and computer vision used to understand which parts of an image are important in neural network decisions. It helps visualize the most critical regions for a convolutional neural network (CNN) to make the final classification decision on an input image. If visualizing instances of misclassification in the results, specifically where the normal class is misjudged as abnormal class 1, the corresponding images can be observed in Figures 3.6 and 3.7. In Examples 1 and 2, the upper curve represents the voltage profile, while the lower curve corresponds to the current profile. Examining the reflected outcomes, there is a tendency for the focal points to exhibit weaker intensity and variations.
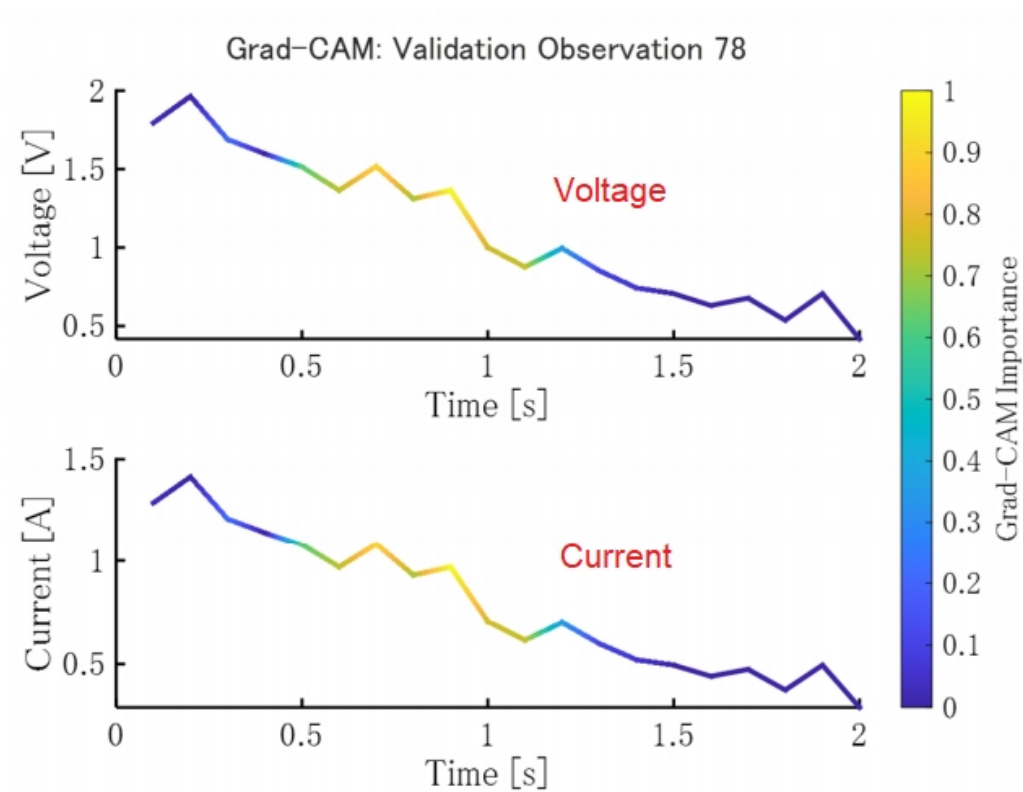
Figure 3.7: Visualization of time response (example 2)

Chapter 4

Cluster Analysis of Heater Wire Breakages

While machine learning methods are highly reliable for detecting heater wire breakages, particularly with a substantial dataset, the practical industrial scenario often involves rare occurrences of specific anomalies like heater wire breakages. In other words, obtaining data for wire breakage conditions is challenging compared to normal operating conditions. This scarcity of wire breakage data compromises the reliability of machine learning methods. In such situations, where limited data availability becomes a bottleneck, a new approach is needed. Data clustering methods successfully address this challenge by enabling effective determination and classification based on a small dataset.

4.1 Data Clustering and Samples Distance

Cluster analysis is an unsupervised machine learning algorithm that categorizes samples based on the similarity of data when no predefined categories are given. Its input consists of a set of unlabeled samples, which are grouped into clusters based on the distance or similarity of the sample data. The objective is to minimize intra-group distances while maximizing inter-group differences [36].

Figure 4.1 presents a simple example of clustered samples where three different colors represent three distinct clusters. The objective of this study is to distinctly differentiate the three conditions of heaters (normal, abnormal 1, abnormal 2) in a similar clear manner to achieve accurate detection.

In cluster analysis, the analysis of distances between samples serves as a crucial and effective metric for learning and classification. In this study, the examination of sample distances is employed as a key indicator to analyze and effectively
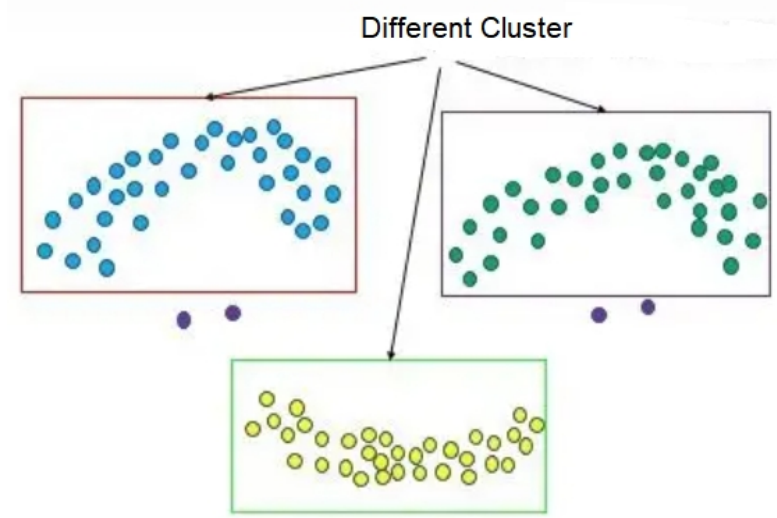
Figure 4.1: Example of clustered samples

detect heater wire breakages.

The most commonly used distances include Euclidean distance, Manhattan distance, Chebyshev distance, Minkowski distance, and Mahalanobis distance, among others. These distances can be represented as illustrated in Figure 4.2, where the distance between the origin and points is equal to 1. In this study, both Euclidean distance and Mahalanobis distance were employed for data analysis.

Euclidean distance, being the most prevalent, is calculated by determining the straight-line distance between two points. It is computed as the square root of the sum of the squares of differences between corresponding dimensions of two points and can be expressed as:

$$D_{Euclidean} = \sqrt{\sum_{i=1}^{n}(x_{2i} - x_{1i})^2} \tag{4.1}$$

where x_{2i} and x_i represent the ith dimension of points 1 and 2, respectively, and the sum is taken over all dimensions (n).

The Euclidean distance is suitable for scenarios characterized by the following features. Firstly, when the clusters in the dataset have an approximately spherical shape or follow a normal distribution, the Euclidean distance serves as a appropri-
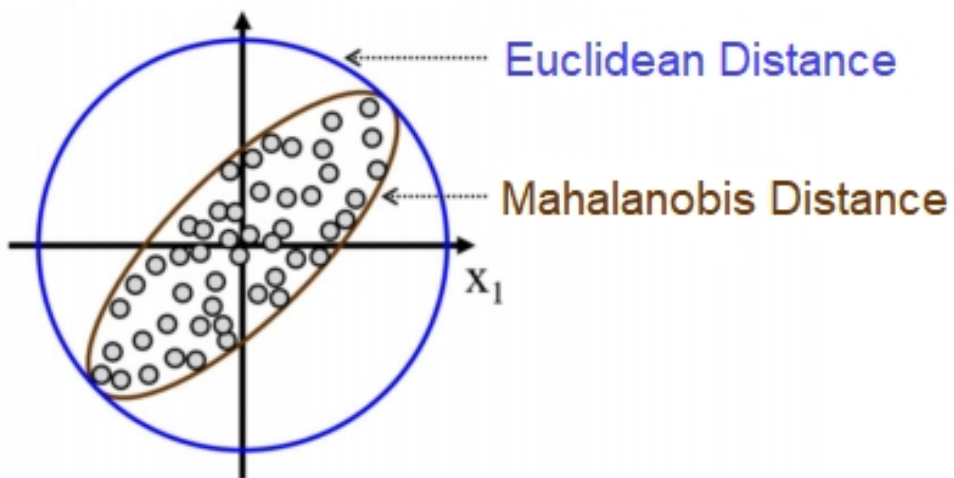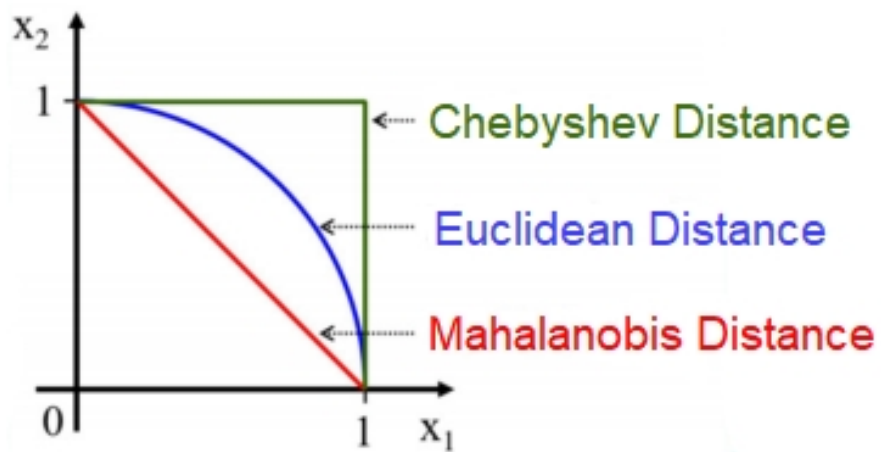
Figure 4.2: Multivariate distances (distance between points and the origin equals 1)

ate metric. Secondly, it proves effective when there is a linear relationship among data features, meaning that the change in one feature is proportionate to the change in other features. Additionally, when the importance of features is similar with no significant weight differences, and the units of each feature are consistent, the Euclidean distance typically performs well. However, in scenarios with irregular data distributions, nonlinear relationships among features, or the presence of outliers, other distance metrics may be more appropriate, as the Euclidean distance tends to be sensitive to such situations. Overall, in scenarios characterized by the mentioned features, the Euclidean distance is a effective choice. However, in specific circumstances, careful consideration of alternative distance metrics is warranted [37].

Mahalanobis distance can be regarded as a modification of the Euclidean distance, addressing issues related to inconsistent and correlated scales among dimensions in Euclidean distance. For two vectors, x and y, the Mahalanobis distance between them can be expressed using the following formula:

$$D_{Mahalanobis} = \sqrt{(x - y)^T \mathbf{S}^{-1}(x - y)} \tag{4.2}$$

where, x and y are vectors representing two sample points, and $\mathbf{S}$ is the covariance matrix.

The computation of the covariance matrix $\mathbf{S}$ is typically based on a dataset. If there is a dataset containing n samples, each with m features, the calculation of the covariance matrix $\mathbf{S}$ is as follows:

$$\mathbf{S} = \frac{1}{n - 1} \sum_{i=1}^{n} (x_i - \bar{x})(x_i - \bar{x})^T \tag{4.3}$$

where, x_i is the vector of the ith sample, and $\bar{x}$ is the mean vector of all samples.

The covariance matrix in Mahalanobis distance is a matrix that represents the relationships between variables. In statistics and machine learning, the covariance matrix is commonly used to describe the correlations and variabilities among multiple random variables. The elements of the covariance matrix represent the covariance between two random variables, and the diagonal elements represent the variances of individual variables. The covariance matrix is a symmetric matrix, where the (i, j) element indicates the covariance between the ith and jth variables.

In Mahalanobis distance, the covariance matrix is applied through its inverse, known as the precision matrix. The precision matrix is the inverse of the covariance matrix and is used to adjust the calculation of Mahalanobis distance, taking into account the correlations between different variables.

The covariance matrix plays a crucial role in Mahalanobis distance by quantifying the relationships between variables, and its inverse (precision matrix) helps in accurately calculating Mahalanobis distance to measure the relative positions of samples in multidimensional space.

4.2   Simulation Model and Parameter Modification

When employing machine learning methods, the subsystem used consists of a model with four parallel heaters. Now, in Figure 4.3, the number of heaters will be expanded to ten while still maintaining a parallel connection. This adjustment will make the diagnostic conditions more stringent and demanding. Moreover, on top of the existing simulation model, white noise interference and step response disturbances have been separately introduced before the output signals. This is done to demonstrate that the system remains stable and can correctly diagnose heater wire breakages even in the presence of external disturbances. The modified simulation model is illustrated in Figure 4.4.

In the figure, the red solid line box represents the step response disturbance. It undergoes a step change to a specified value at a designated moment and utilizes an integrator to simulate its decay process. Consequently, after the step, it will gradually decay to zero over a certain period of time. As shown in Figure 4.5, this is the waveform output of the step response disturbance.

The new experimental approach follows three main aspects:

1. Compute estimated values for temperature and resistance.

2. Utilize the covariance matrix learned from normal data to calculate the Euclidean distance and Mahalanobis distance for the estimated temperature and resistance values.

3. Diagnose heater wire breaks based on the deviation between the data and normal values.
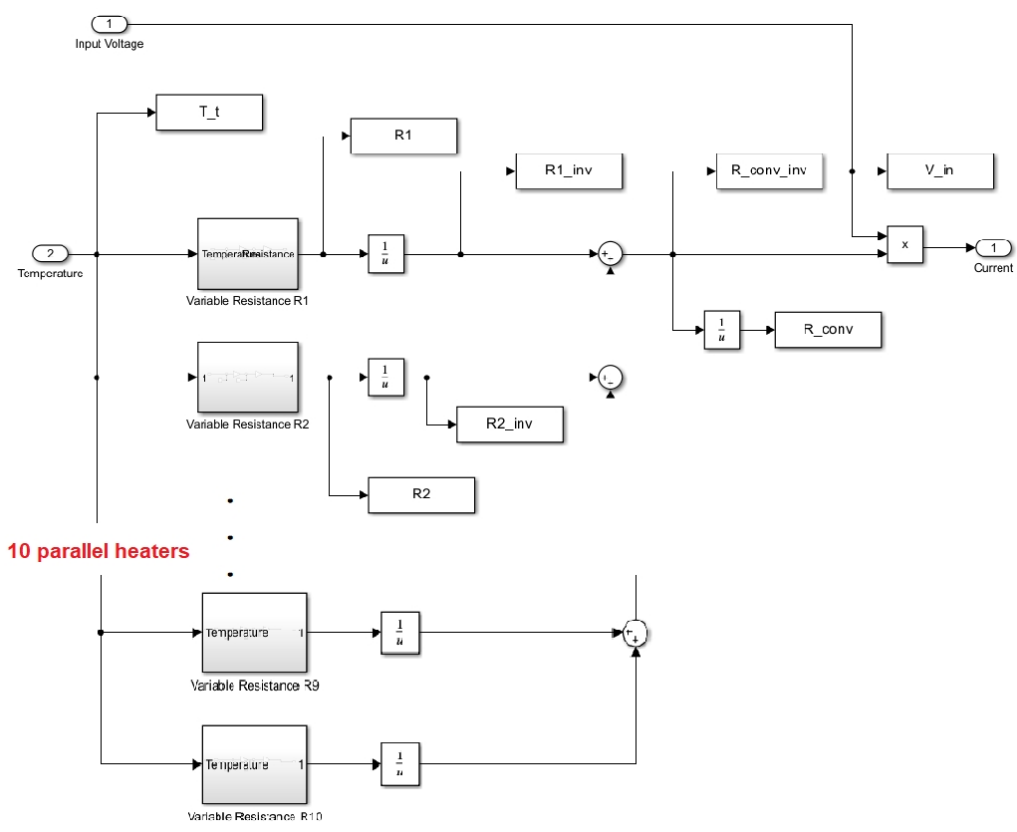
Figure 4.3: Subsystem of 10 parallel heaters
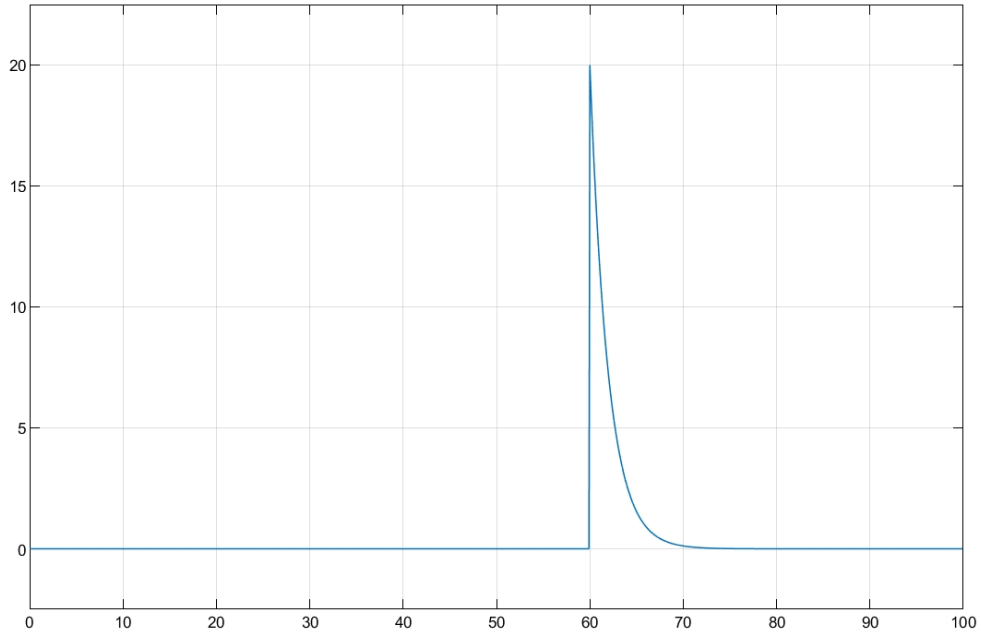
Figure 4.4: Waveform of Disturbance
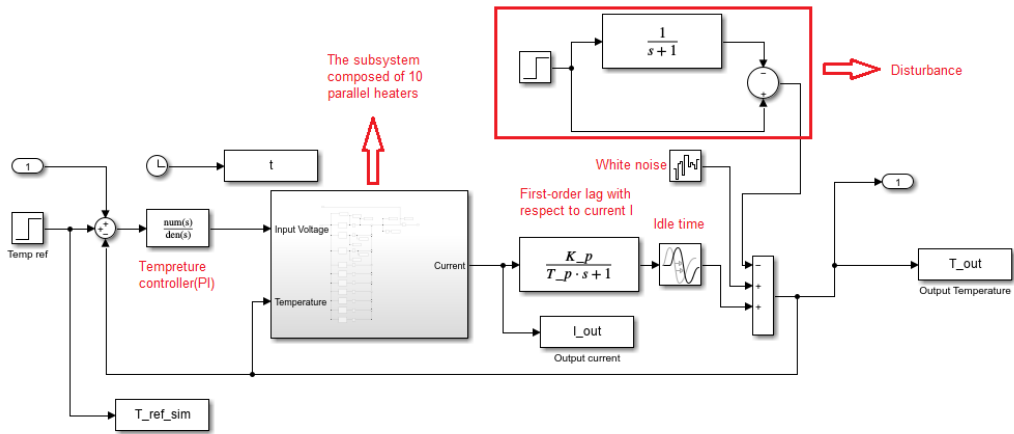
Figure 4.5: Modified simulation model

Upon the foundation of the original simulation data, white noise is set to follow a normal distribution with a variance of 0.1. The amplitude of the step response disturbance is designated as 20, and it will undergo a step change at 60 seconds, decaying to 0 within 10 seconds (thus returning to normal).

On the existing foundation of machine learning and detection parameters, the data acquisition method is modified as follows: within 40 seconds after the response to the step response disturbance, randomly select 2 seconds of data for detection. The input signal is modified to be the average temperature T_{ave} and the average resistance R_{ave}. The calculation methods for T_{ave} and R_{ave} are given by the following formulas:

$$T_{ave} = \frac{1}{n} \sum_{k=1}^{n} T_k \tag{4.4}$$

$$R_{ave} = \frac{\frac{1}{n} \sum_{k=1}^{n} v_k}{\frac{1}{n} \sum_{k=1}^{n} i_k} \tag{4.5}$$

Where T_k, v_k, and i_k represent the collected temperature, voltage, and current data, respectively, and n is the number of data points. As 2 seconds of data are randomly selected, there will be 20 data points, so the value of n is set to 20. And $\frac{1}{n} \sum_{k=1}^{n} v_k$ is the calculation of average of voltage, while $\frac{1}{n} \sum_{k=1}^{n} i_k$ is of current.

4.3 Simulation Results

4.3.1 Graphical output of collected data

After modifying the simulation model and various parameters, run the simulation without applying the step response disturbance. Observe the temperature variation curves for three different scenarios, as shown in Figure 4.6. From left to right, these represent the normal, abnormal 1, and abnormal 2 scenarios of heater wire breakage. It is clear from the figures that the wire breakage in the heater (i.e., increased resistance) causes a delayed and weakened temperature rise.

After observing the temperature variation without external disturbances, let's introduce a disturbance and run the simulation. Obtain the temperature variation curve under normal conditions, as shown in Figure 4.6. The dashed line indicates
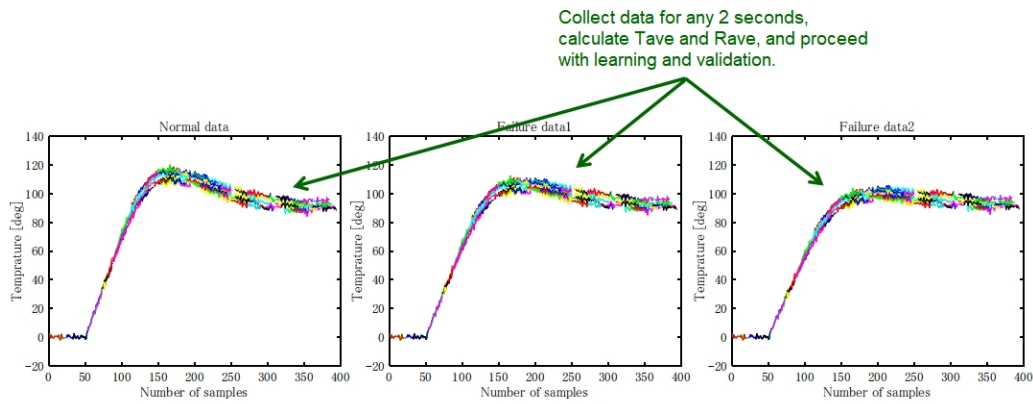
Figure 4.6: Temperature output curves

the time point when the disturbance is applied, which is the time point of the step response.

Similarly, calculating the average resistance value requires voltage and current data. To establish an overall observation of the data, output the curves of voltage and current with the changing number of wire breakages, as shown in Figure 4.8. Again, from left to right, the wire breakage scenarios are normal, anomaly 1, and anomaly 2. The red curve represents the voltage curve, while the blue curve represents the current curve. Through the graphs, two observations can be made:

1. The lower limit and decay characteristics of the voltage are different.

2. The current values decrease in the order of normal, anomal 1, and anomal 2.

Then, calculate the average resistance value using the mean voltage and mean current.

In the process of calculating the average resistance value and presenting it alongside the average temperature value as functions of the data quantity, it's aimed to derive insightful curves that showcase the relationship between these two essential parameters. These curves serve as valuable features in subsequent analyses, particularly in the computation of Euclidean distance and Mahalanobis distance. By aligning the vertical axis scales across these curve coordinate systems, a coherent and comprehensive visualization emerges, facilitating a nuanced understanding of the interplay between the average resistance and temperature
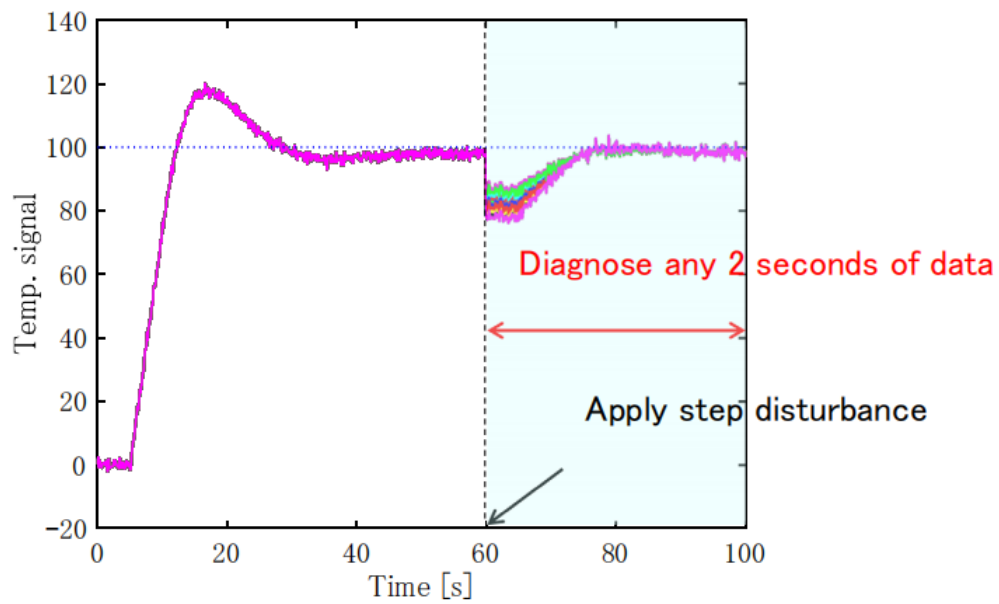
Figure 4.7: Time response of T(normal)
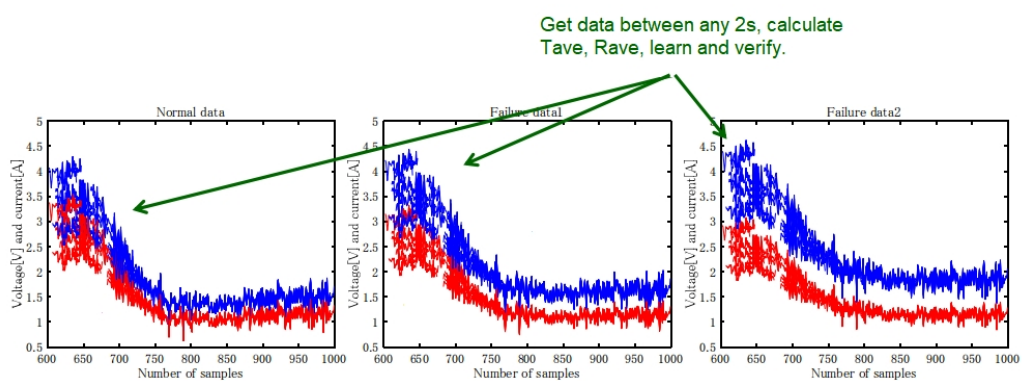
Figure 4.8: Time response curves of voltage and current

31

values. This meticulous exploration enables us to glean valuable insights into the nuanced behaviors of the system under varying conditions, enhancing ability to discern patterns and anomalies in the data.

As illustrated in Figure 4.9, the curves depict the post-output graphs of average temperature values and average resistance values. From left to right, the scenarios represent normal, abnormal 1, and abnormal 2 conditions, each associated with a distinct heater wire breakage situation. The upper curves represent the trends in average resistance values, while the lower curves showcase the patterns in average temperature values. This visual representation offers a comprehensive insight into the dynamics of the system under different heater wire breakage scenarios, providing a clear distinction between normal and abnormal conditions.

From the graphs, the following observations can be made:

1. The average resistance values increase with the number of heaters under wire breakage.

2. The average temperature values decrease with the number of heaters under wire breakage (as wire breakage represents temperatures exceeding the threshold, indicating a reduction in the quantity of data exceeding the threshold).

4.3.2   Calculation and graphical output of distances

On the basis of the above data curve images, distance values for feature quantities are calculated, combined with the average resistance values and average temperature values, and output as a two-dimensional sample distribution graph.

For better observation, the two-dimensional plot separates the learning data from the testing data.

As shown in Figure 4.10, it represents the two-dimensional plot of learning data (average resistance value R_{ave} and average temperature value T_{ave}) under normal conditions. In the graph, each black hollow point represents a data sample, and the blue "x" point denotes the centroid calculated by the Euclidean distance, which is also the average point of the data.

As shown in Figure 4.11, it is a two-dimensional distribution map of detection data (Average Resistance Value R_{ave} and Average Temperature Value T_{ave}) in
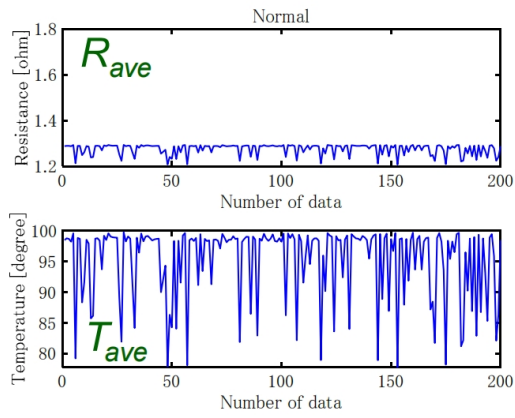
(a) Normal (a)
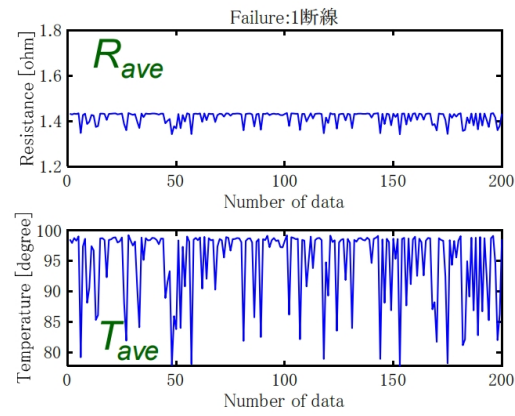
(b) Abormal 1 (b)
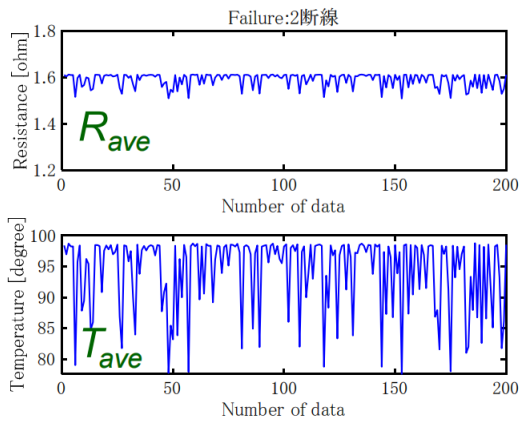
(c) Abnormal 2 (c)

Figure 4.9: Coordinated comparison of average resistance values and average temperature values
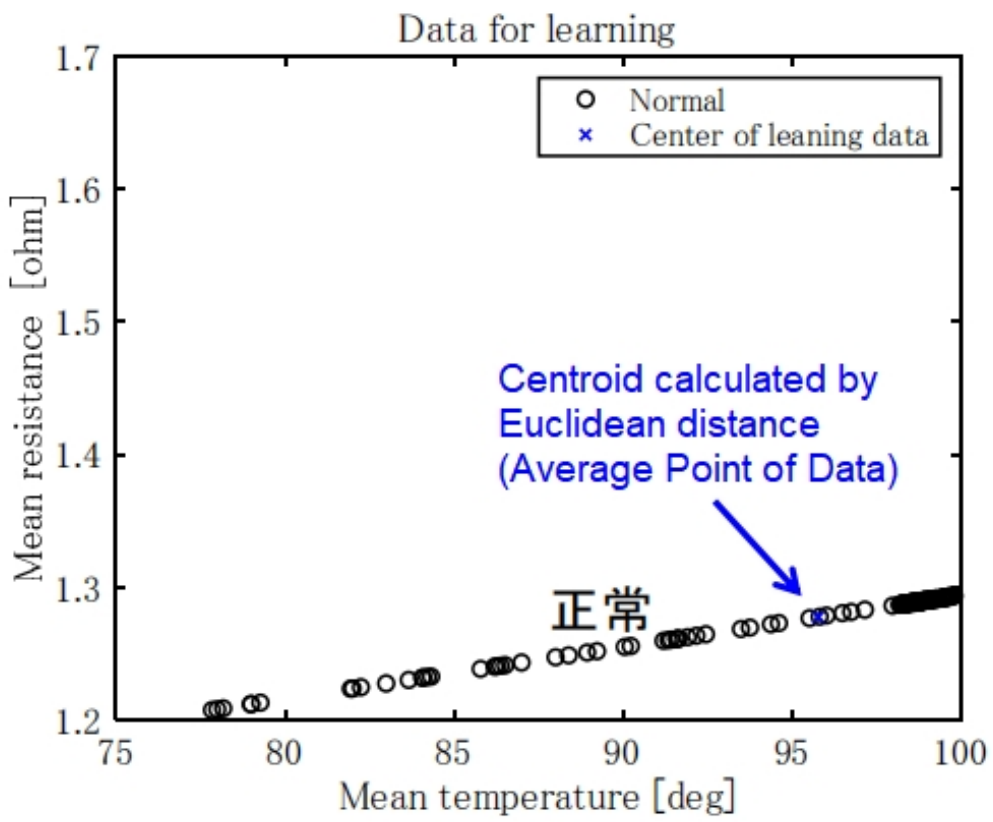
Figure 4.10: Average resistance and average temperature (learning data)
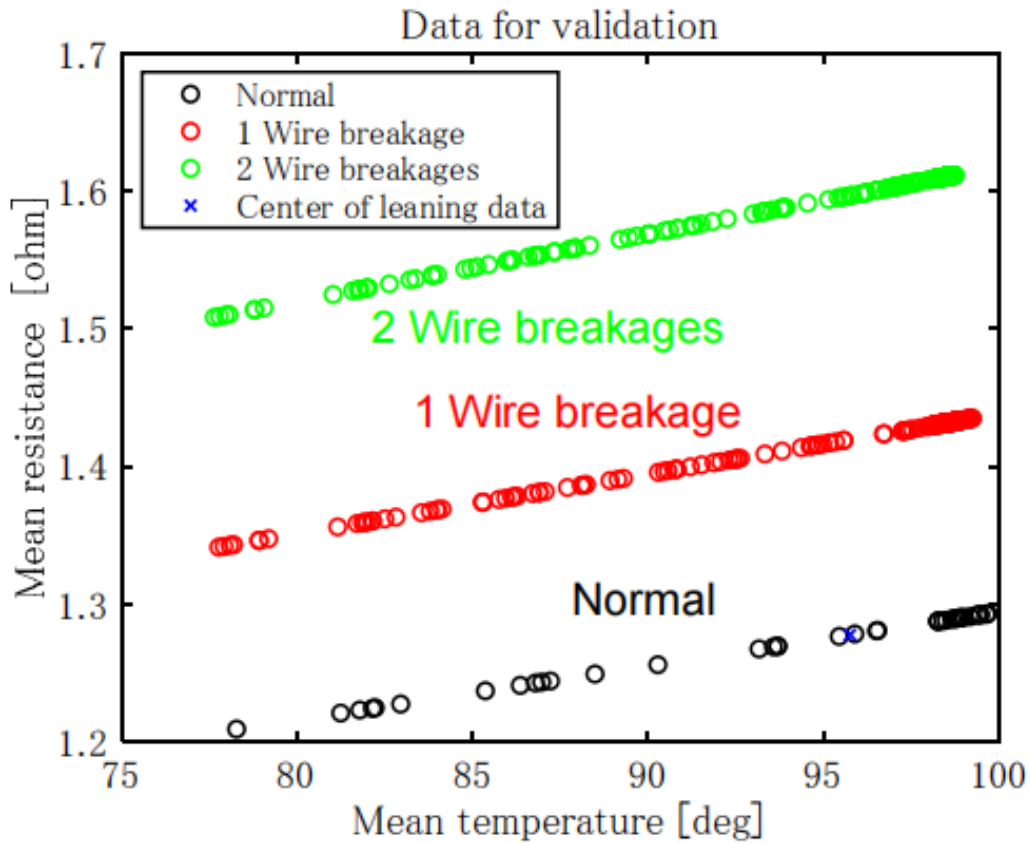
Figure 4.11: Average resistance and average temperature (validation data)

three scenarios. In the figure, black, red, and green hollow points represent the distribution under normal, abnormal 1, and abnormal 2 conditions, respectively. Similar to the image of learning data, the blue "x" point is the centroid calculated by Euclidean distance, which is also the average point of the data.

From Figures 4.10 and 4.11, the following observations can be made:

1. The average resistance increases with the number of broken heaters.

2. In the normal case, there are more instances exceeding the temperature threshold, and there are also data points at higher temperatures.

3. No zero division due to current, and little variability in the features.

Next, calculate the Euclidean distance and Mahalanobis distance from the col-

lected data. In this study, these data points are all in a two-dimensional plane, so we only need to consider the two-dimensional calculation methods. The general formulas for Euclidean distance and Mahalanobis distance in multi-dimensional space have been discussed earlier (Equations 4.1 and 4.2). Here, we simplify them to two-dimensional formulas:

$$D_{Euclidean} = \sqrt{X^2 + Y^2} \tag{4.6}$$

$$D_{Mahalanobis} = \frac{1}{2} \begin{bmatrix} X & Y \end{bmatrix} \begin{bmatrix} 1 & r \\ r & 1 \end{bmatrix}^{-1} \begin{bmatrix} X \\ Y \end{bmatrix} \tag{4.7}$$

where, X and Y represent the horizontal and vertical coordinates of the data sample points, respectively. The variable r in Mahalanobis distance denotes the correlation coefficient.

Thus, the distribution of Euclidean distances for the samples is illustrated in Figure 4.12. Here, black represents the normal condition, red represents the abnormality 1 condition (1 heater wire breakage), and green represents the abnormality 2 condition (2 heater wire breakages). From the image, it can be observed that within a certain data range (between 0 and 0.05), the Euclidean distances of the samples exhibit a concentrated block, indicating a significant clustering of distances in this range. However, it is evident that there is a problem as there is no clear distinction or boundary line among the Euclidean distances of the three conditions. This lack of clear separation makes it challenging to use machine learning for wire breakage diagnosis. This is because there are a considerable number of outliers among the samples. Once there are many outliers, the calculation accuracy of the Euclidean distance rapidly decreases, resulting in an irregular and undistinguished distribution of distance data. Therefore, using the Euclidean distance is not suitable for this study.

Similarly, calculating the Mahalanobis distance results in the sample distribution plot shown in Figure 4.13.

The classification of the sample points in black, red, and green corresponds to the performance of the Mahalanobis distance, where black represents normal, red represents anomaly 1, and green represents anomaly 2. It can be observed that in the calculated Mahalanobis distance, normal data (black) is concentrated between 0 and 5. Due to the larger magnitude, the Mahalanobis distance distribution of normal data samples is shown in an enlarged view within the dashed box.

36
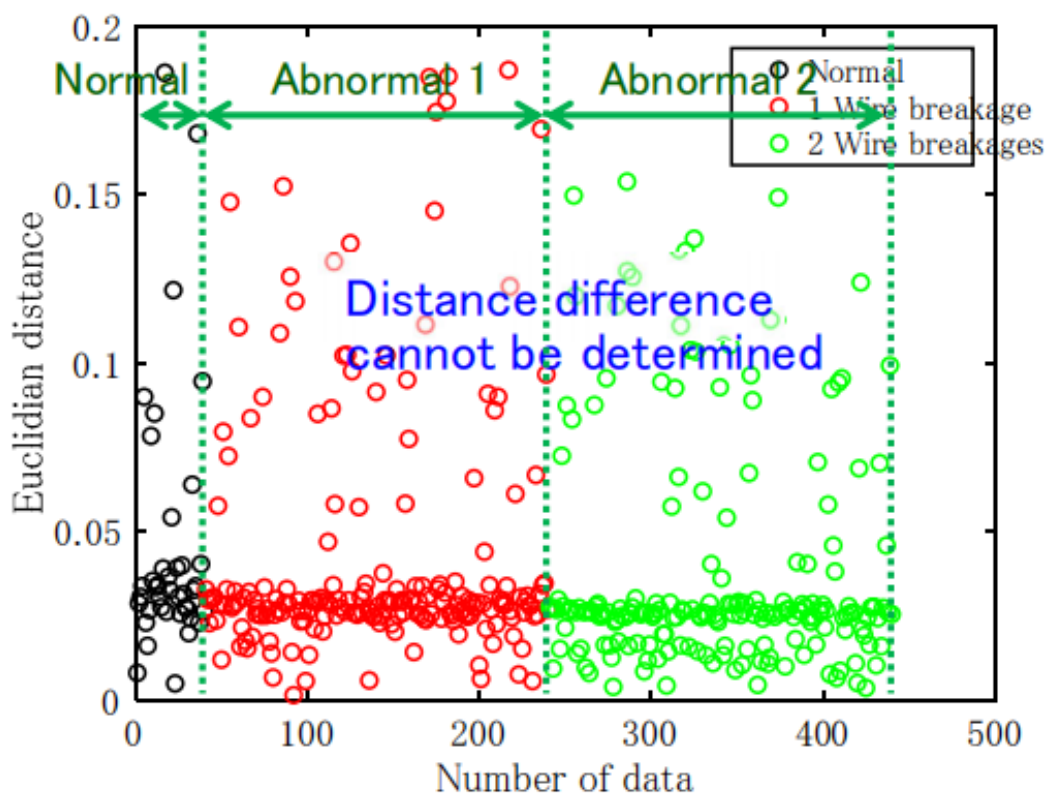
Figure 4.12: Euclidean distance
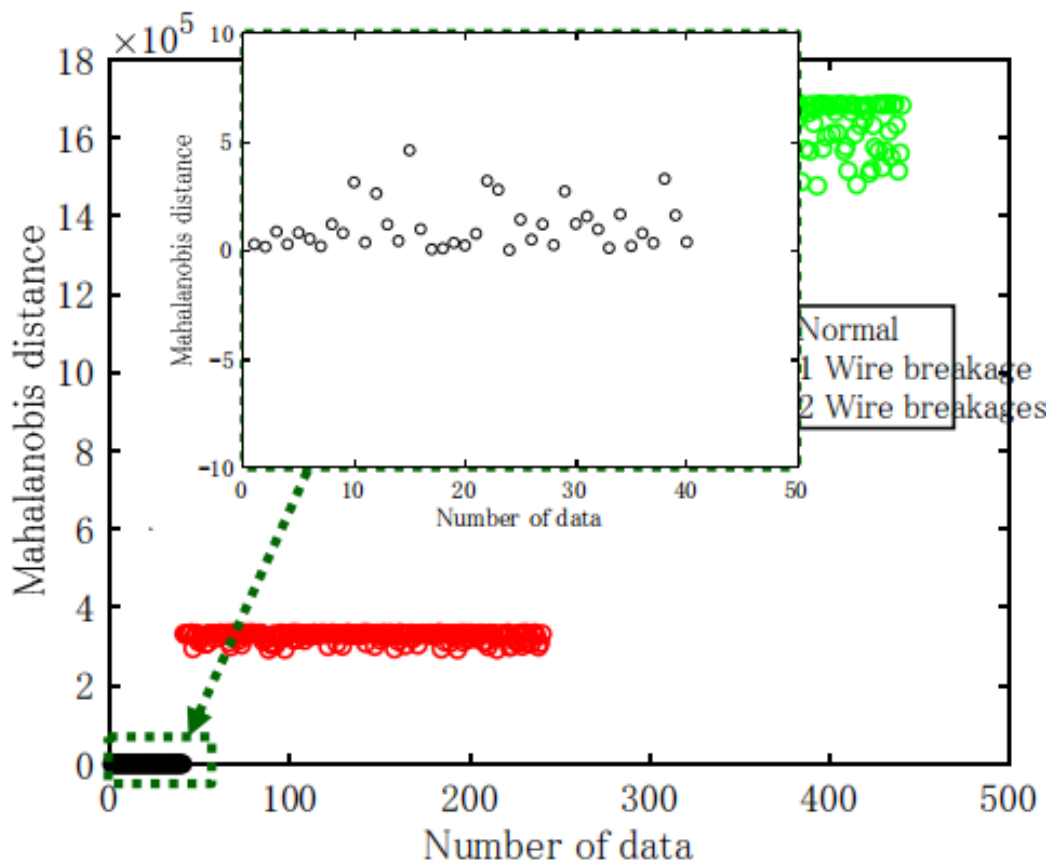
Figure 4.13: Mahalanobis distance

Anomaly 1 data (red) is mainly distributed around 3×10^5, and anomaly 2 data (green) is primarily distributed between 14×10^5 and 18×10^5.

Here, it can be observed that using Mahalanobis distance, with an appropriate threshold, not only perfectly distinguishes the three different wire breakage scenarios but also achieves a significantly large separation in distance magnitudes. This not only addresses the issue of insufficient wire breakage data but also provides a better means to detect whether a heater is broken in practical industrial production.

Chapter 5

Exploration of Factors Affecting Mahalanobis Distance

5.1   Predicting Factors Influencing Mahalanobis Distance

Mahalanobis distance is subject to the influence of various factors, especially in multivariate scenarios, which can affect its effectiveness and interpretability. The following factors are prone to impact Mahalanobis distance:

1. **Covariance Matrix**: The structure of the covariance matrix $\mathbf{S}$ significantly influences Mahalanobis distance calculations. Changes or variations in this matrix can have a substantial impact on distance measurements.

2. **Outlier Handling**: Sensitivity to outliers is a critical consideration for Mahalanobis distance. Strategies for identifying and handling outliers are crucial to prevent distorted distance measurements.

3. **Correlation among features**: Mahalanobis distance assumes correlations between different features. Understanding the nature and strength of these correlations is essential for accurate distance calculations.

4. **Dimensionality of data**: The effectiveness of Mahalanobis distance may vary with the dimensionality of the dataset. High-dimensional spaces present challenges, and the curse of dimensionality can impact reliability.

5. **Sample size**: The size of the dataset influences Mahalanobis distance performance. Limited samples may require regularization techniques or alternative distance metrics to address issues related to the inversion of the covariance matrix.

6. **Normality assumption**: Mahalanobis distance calculations assume multivariate normality. Deviations from this assumption can impact measurement accuracy, necessitating adaptations if the data distribution is substantially non-normal.

7. **Threshold selection**: Establishing an appropriate threshold for Mahalanobis distance is crucial for classification or anomaly detection. Optimal threshold determination involves balancing false positives and false negatives, often requiring iterative adjustments.

In Chapter 4, this paper has already introduced the covariance matrix, which is a crucial factor for Mahalanobis distance. Outlier handling is a common step in data analysis and statistics, aiming to identify and manage exceptional values or outliers within a dataset. Outliers refer to data points that significantly differ from other data points, and they can arise due to measurement errors, data entry mistakes, system malfunctions, or genuinely rare events. In this study, the analysis of data dimensions is not necessary since all data points in this research are two-dimensional samples.

The normality assumption is a commonly used assumption in statistics, indicating that the distribution of data follows a normal distribution (or Gaussian distribution). Under this assumption, the data forms a bell-shaped curve, with the mean, median, and mode being equal. The normality assumption is crucial for the effectiveness of many statistical methods and inferences because some statistical methods require the data to satisfy the assumption of normal distribution for effective parameter estimation and hypothesis testing. However, in practical applications, data may not always conform perfectly to a normal distribution. Therefore, in research, the normality of data is typically tested using statistical methods or alternative methods that are less sensitive to the assumption of normality.

In this study, a detailed exploration of threshold selection is not undertaken. Instead, the investigation focuses on the impact of parameters and variables from the simulation on the output results of the Mahalanobis distance.

5.2 The Impact of Time Duration on Mahalanobis Distance

To elaborate on the impact of varying the Time Duration parameter, it is essential to understand its significance in the context of the simulation framework.

Time Duration serves as a critical variable that determines the temporal span over which data is sampled during the simulation process. This temporal sampling is particularly crucial in capturing the dynamic behavior of the system under investigation.

In the realm of this research, where the simulation involves the collection of data points at a rate of 0.1 seconds, the Time Duration parameter plays a pivotal role in shaping the granularity of the collected data. A nuanced exploration of the Mahalanobis Distance is facilitated by manipulating the Time Duration setting, allowing for a more comprehensive analysis of how variations in temporal sampling influence the output of the Mahalanobis Distance metric. By defining Time Duration as x seconds, the research aims to systematically investigate how alterations in this temporal parameter impact the Mahalanobis Distance.

Now, it is planned to set the Time Duration parameter to 0.2 seconds, 0.5 seconds, 1 second, 2 seconds, and 5 seconds, respectively, to systematically observe the variations in the distribution of Mahalanobis Distance. Since previous experiments have already investigated the case where Time Duration is set to 2 seconds, there is no need to replicate the experiment for this specific duration.

As shown in Figure 5.1, the data distribution plot is obtained when the Time Duration is set to 0.2 seconds. In the plot, black represents normal sample points, red represents samples with anomaly 1, and green represents samples with anomaly 2. Due to the very short Time Duration, the data volume is significantly reduced compared to the 2-second duration. Under this condition, successfully classifying these data points demonstrates the reliability and stability of the heater wire breakage diagnostic system.

Not only that, but it can be observed that the data distribution has also changed compared to the previous experiment, being more concentrated in the range of temperatures above 85. Next, the distribution of Mahalanobis distances is presented in Figure 5.2.

Next, change the time duration values to 0.5 seconds, 1 second, and 5 seconds, respectively, and repeat the above experiment. Under different time duration conditions, calculate the mean Mahalanobis distance for the normal, abnormal 1, and abnormal 2 situations. Output the results as a line chart, as shown in Figure 5.3. Here, the meanings of the black, red, and green data points are the same as before. The horizontal axis represents the set values of the time duration, while the vertical axis represents the mean Mahalanobis distance. Each endpoint of a different-colored line represents the mean Mahalanobis distance under the corre-
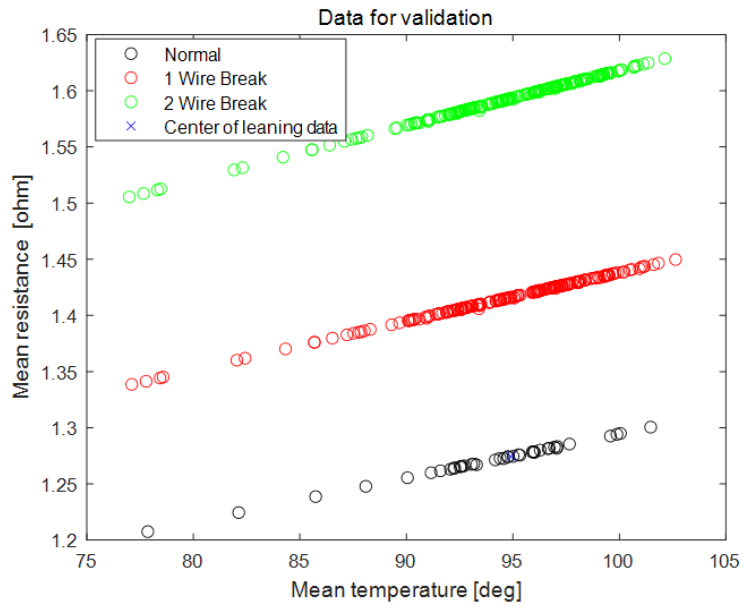
Figure 5.1: Data distribution when time duration is 0.2 Seconds
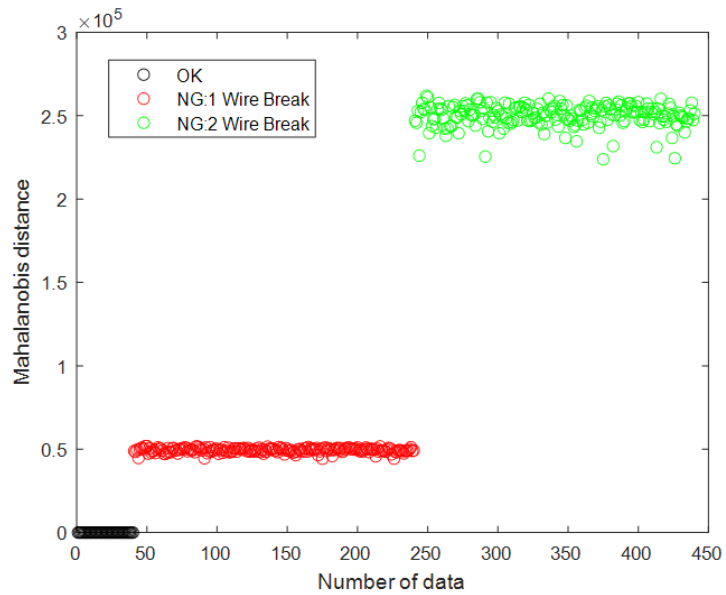
Figure 5.2: Mahalanobis distance distribution for time duration of 0.2 seconds

43
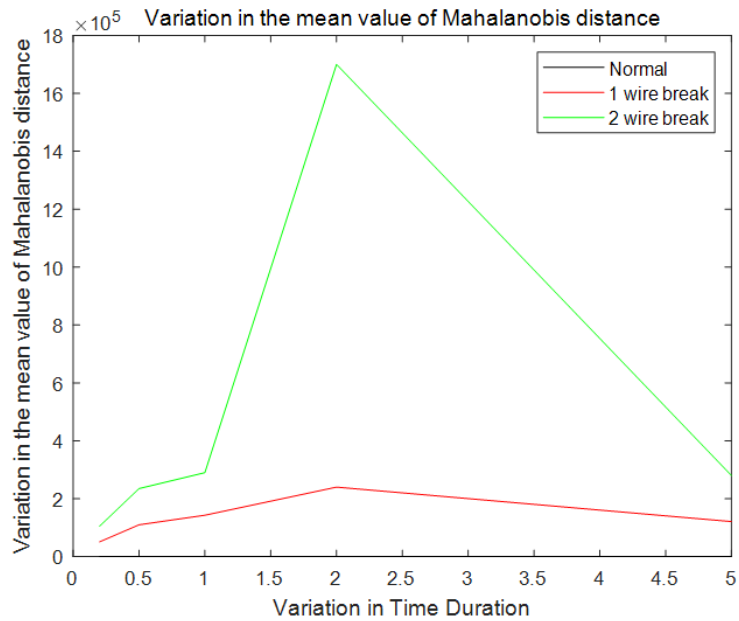
Figure 5.3: Variation in the mean value of Mahalanobis distance while time duration ranging

sponding color condition for the set time duration value.

It can be observed that the value of the time duration does indeed have an impact on the Mahalanobis distance, but the regularity of the changes is not well-reflected among these values.

5.3 The Impact of the Amplitude of Disturbance on Mahalanobis Distance

Considering that when external disturbances are applied, the amplitude of the step response (i.e., the intensity of the disturbance) also affects the collected data, the next part of the study is to examine the influence of this amplitude on the final Mahalanobis distance. Therefore, a controlled variable method should still be employed, by changing the amplitude values of the disturbance to 2, 5, 10, 20 while keeping the time duration at 2 seconds, to observe the variation in Mahalanobis distance.

The previous experiments have already explained the case with an amplitude
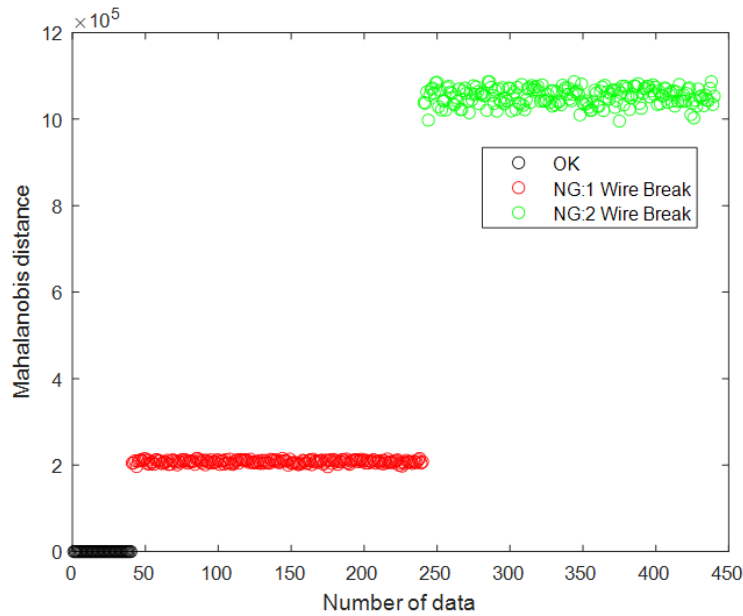
Figure 5.4: Mahalanobis distance distribution for amplitude of disturbance of 10

of 20. Similarly, there will be no repetition of the experiment. Now, the Mahalanobis distance distribution obtained with an amplitude of 10 will be directly presented, as shown in Figure 5.4.

From the illustrated content, it can be observed that in the case of anomaly 1, the mean Mahalanobis distance is around 2.1×10^5, while in the case of anomaly 2, the mean Mahalanobis distance is around 11.6×10^5. Subsequently, by continuing to change the amplitude values to 5 and 2, obtaining the corresponding Mahalanobis distance distributions and data, calculating the mean Mahalanobis distance, and outputting the line chart for different amplitude conditions as shown in Figure 5.5.

From the content in the figure, it can be observed that when the amplitude of the step response disturbance changes, the mean Mahalanobis distance also changes, showing a positive correlation trend. In other words, the mean Mahalanobis distance increases with the increase in the amplitude of the external disturbance.
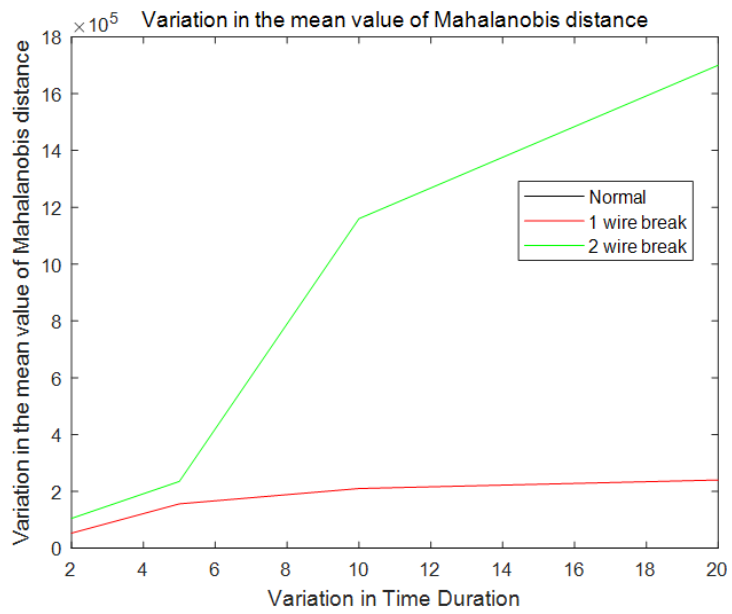
Figure 5.5: Variation in the mean value of Mahalanobis distance while the amplitude of disturbance ranging

Chapter 6

Conclusion

This paper investigated the detection method for the occurrence of temperature anomalies and disconnection in the heating system of a temperature control system. Several conclusions were drawn from the research. Firstly, in the temperature control system, diagnosing the disconnection of the heater using traditional machine learning methods is feasible. With a sufficient amount of data, accurate results can be obtained. However, obtaining a substantial number of abnormal data points is challenging in practical industrial production. Therefore, the use of data clustering analysis methods can effectively address this issue. Upon computing the Euclidean distance and Mahalanobis distance for the collected heater data, it was found that the Euclidean distance does not differentiate well between the three disconnection scenarios as effectively as the Mahalanobis distance. The Mahalanobis distance, utilizing its eigenvector properties, distinctly classifies the three situations: normal, abnormal 1 (one heater wire breakage), and abnormal 2 (two heaters wire breakages). Finally, in the exploration of factors affecting Mahalanobis distance, this study discovered that time duration does influence Mahalanobis distance, although the regularity of this influence is not prominent. Additionally, the amplitude of the step response disturbance also affects Mahalanobis distance, and the mean Mahalanobis distance increases with the amplitude's augmentation.

In conclusion, this research provides valuable insights into the diagnosis of heater disconnection in a temperature control system. The Mahalanobis distance, particularly when accounting for factors like time duration and disturbance amplitude, proves to be an effective and reliable method for classifying different disconnection scenarios in the absence of abundant abnormal data in practical industrial settings.

Q&A

Q: In page 11, how did you defined parameter of time delay τ and time constant t (First-delay)?
A: The time delay τ was identified by the schematic of the system. From the system, the relationship of resistance and temperature was shown. And based on it, it could be found that how long it took to rise the temperature to a certain value. So the time delay and base temperature could be calculated and defined.

Q: What is T and t?
A: In this research, t represents the base temperature, and T represents the real time temperature. And there is a linear relationship between the two parameters.

Q: Were you the one who specified the t?
A: Yes. I specified the base temperature t. The t was specified to indicate a base temperature so that the base resistance would be able to calculated. Based on it, the real time temperature T could be calculated and collected.

Reference

[1] D.C. Guo. Application of thermoelectric cooler in temperature control system of space science experiment. *Applied Thermal Engineering*, 168, 2020.

[2] Y.Y. Liang, D.D. Wang, and J.P. Chen. Temperature control for a vehicle climate chamber using chilled water system. *Applied Thermal Engineering*, 106:117–124, 2016.

[3] Mingming Mao and Junrui Shi. Experimental investigation on control of temperature asymmetry and nonuniformity in a pilot scale thermal flow reversal reactor. *Applied Thermal Engineering*, 175, 2020.

[4] Yanxiang Jia and Yingshu Liu. Refrigerating characteristics of ice storage capsule for temperature control of coal mine refuge chamber. *Applied Thermal Engineering*, 75:756–762, 2015.

[5] Marco Cespi, Giulia Bonacucina, Luca Casettari, Sara Ronchi, and Giovanni Filippo Palmieri. Effect of temperature increase during the tableting of pharmaceutical materials. *International Journal of Pharmaceutics*, 448(1):320–326, 2013.

[6] Siu Ki Lau and Siu Kwong Ho. Open-circuit fault detection in distribution overhead power supply network. *Journal of International Council on Electrical Engineering*, 7(1):269–275, 2017.

[7] Zhiwei Gao, Carlo Cecati, and Steven X. Ding. A survey of fault diagnosis and fault-tolerant techniques—part i: Fault diagnosis with model-based and signal-based approaches. *IEEE Transactions on Industrial Electronics*, 62(6):3757–3767, 2015.

[8] D. U. Campos-Delgado and D. R. Espinoza-Trejo. An observer-based diagnosis scheme for single and simultaneous open-switch faults in induction motor drives. *IEEE Transactions on Industrial Electronics*, 58(2):671–679, 2011.

[9] M. Salehifa, N. R. N. Idris, and M. J. A. Aziz. Fpga based robust open transistor fault diagnosis and fault tolerant sliding mode control of five-phase pm motor drives. *J. Power Electron.*, 15(1):131–145, 2015.

[10] Shin-Myung Jung, Jin-Sik Park, Hag-Wone Kim, Kwan-Yuhl Cho, and Myung-Joong Youn. An mras-based diagnosis of open-circuit fault in pwm voltage-source inverters for pm synchronous motor drive systems. *IEEE Transactions on Power Electronics*, 28(5):2514–2526, 2013.

[11] Qun-Tao An, Li Sun, and Li-Zhi Sun. Current residual vector-based open-switch fault diagnosis of inverters in pmsm drive systems. *IEEE Transactions on Power Electronics*, 30(5):2814–2827, 2015.

[12] Bin Gou, Xinglai Ge, Shunliang Wang, Xiaoyun Feng, James B. Kuo, and Thomas G. Habetler. An open-switch fault diagnosis method for single-phase pwm rectifier using a model-based approach in high-speed railway electrical traction drive system. *IEEE Transactions on Power Electronics*, 31(5):3816–3826, 2016.

[13] Christopher Brunson, Lee Empringham, Liliana De Lillo, Patrick Wheeler, and Jon Clare. Open-circuit fault detection and diagnosis in matrix converters. *IEEE Transactions on Power Electronics*, 30(5):2840–2847, 2015.

[14] Chuang Liu, Lei Kou, Guowei Cai, Zihan Zhao, and Zhe Zhang. Review for ai-based open-circuit faults diagnosis methods in power electronics converters. *ArXiv*, abs/2209.14058, 2022.

[15] Surin Khomfoi and Leon M. Tolbert. Fault diagnosis and reconfiguration for multilevel inverter drive using ai-based techniques. *IEEE Transactions on Industrial Electronics*, 54(6):2954–2968, 2007.

[16] Zhanjun Huang, Zhanshan Wang, and Huaguang Zhang. Multiple open-circuit fault diagnosis based on multistate data processing and subsection fluctuation analysis for photovoltaic inverter. *IEEE Transactions on Instrumentation and Measurement*, 67(3):516–526, 2018.

[17] Zhicheng Ji Yanxia Shen, Wenjing Zhou et al. Fault diagnosis of converter used in wind power generation based on wavelet packet analysis and svm. *Acta Energiae Solaris Sinica*, 36(4):785–791, 2015.

[18] Indrayudh Bandyopadhyay, Prithwiraj Purkait, and Chiranjib Koley. Performance of a classifier based on time-domain features for incipient fault detection in inverter drives. *IEEE Transactions on Industrial Informatics*, 15(1):3–14, 2019.

[19] Mengshi Li, Da Yu, Ziming Chen, Kaishun Xiahou, Tianyao Ji, and Q. H. Wu. A data-driven residual-based method for fault diagnosis and isolation

in wind turbines. *IEEE Transactions on Sustainable Energy*, 10(2):895–904, 2019.

[20] Yanqing Peng Huaqing Xu and Lumei Su. Research on open circuit fault diagnosis of inverter circuit switching tube based on machine learning algorithm. *IOP Conference Series: Materials Science and Engineering*, 452(4):042015, 2018.

[21] Shibo Lu, Tharmakulasingam Sirojan, B. T. Phung, Daming Zhang, and Eliathamby Ambikairajah. Da-dcgan: An effective methodology for dc series arc fault diagnosis in photovoltaic systems. *IEEE Access*, 7:45831–45840, 2019.

[22] Marco Rigamonti, Piero Baraldi, Enrico Zio, Allegra Alessi, Daniel Astigarraga, and Ainhoa Galarza. Identification of the degradation state for condition-based maintenance of insulated gate bipolar transistors: A self-organizing map approach. *Microelectronics Reliability*, 60:48–61, 2016.

[23] Qichen Yang, Jiangchao Qin, and Maryam Saeedifard. Analysis, detection, and location of open-switch submodule failures in a modular multilevel converter. *IEEE Transactions on Power Delivery*, 31(1):155–164, 2016.

[24] Jianhua Qin and Li Wang. Research on diagnostic method of spacecraft electrical power system based on variable weight hierarchical principal component analysis. *Chinese Journal of Scientific Instrument*, 39(8):15–23, 2018.

[25] Baoping Cai, Yubin Zhao, Hanlin Liu, and Min Xie. A data-driven fault diagnosis methodology in three-phase inverters for pmsm drive systems. *IEEE Transactions on Power Electronics*, 32(7):5590–5600, 2017.

[26] Serkan Kiranyaz, Adel Gastli, Lazhar Ben-Brahim, Nasser Al-Emadi, and Moncef Gabbouj. Real-time fault detection and identification for mmc using 1-d convolutional neural networks. *IEEE Transactions on Industrial Electronics*, 66(11):8760–8771, 2019.

[27] Sheng Lan, Mou-Jie Chen, and Duan-Yu Chen. A novel hvdc double-terminal non-synchronous fault location method based on convolutional neural network. *IEEE Transactions on Power Delivery*, 34(3):848–857, 2019.

[28] Tiancheng Shi, Yigang He, Tao Wang, and Bing Li. Open switch fault diagnosis method for pwm voltage source rectifier based on deep learning approach. *IEEE Access*, 7:66595–66608, 2019.

[29] Yigang He, Chenchen Li, Tao Wang, Tiancheng Shi, Lin Tao, and Weibo Yuan. Incipient fault diagnosis method for igbt drive circuit based on improved sae. *IEEE Access*, 7:92410–92418, 2019.

[30] Suliang Ma, Mingxuan Chen, Jianwen Wu, Yuhao Wang, Bowen Jia, and Yuan Jiang. High-voltage circuit breaker fault diagnosis using a hybrid feature transformation approach based on random forest and stacked autoencoder. *IEEE Transactions on Industrial Electronics*, 66(12):9777–9788, 2019.

[31] Behrooz Mirafzal and Sanjoy Das. Condition monitoring and fault-tolerance agents for grid-tied inverters. In *2012 IEEE Power and Energy Society General Meeting*, pages 1–3, 2012.

[32] Zhichun Yang, Yu Shen, Fan Yang, and et al. A transfer learning fault diagnosis model of distribution transformer considering multi-factor situation evolution. *Transactions of China Electrotechnical Society*, 34(7):1505–1515, 2019.

[33] Serkan Kiranyaz, Turker Ince, Osama Abdeljaber, Onur Avci, and Moncef Gabbouj. 1-d convolutional neural networks for signal processing applications. pages 8360–8364, 2019.

[34] Alex Krizhevsky, Ilya Sutskever, and Geoffrey E. Hinton. Imagenet classification with deep convolutional neural networks. *Commun. ACM*, 60(6):84–90, may 2017.

[35] James T Townsend. Theoretical analysis of an alphabetic confusion matrix. *Perception & Psychophysics*, 9:40–50, 1971.

[36] Wolfgang Vogt and Dorothea Nagel. Cluster Analysis in Diagnosis. *Clinical Chemistry*, 38(2):182–198, 02 1992.

[37] T. Soni Madhulatha. An overview on clustering methods. *CoRR*, abs/1205.1117, 2012.

List of Publications

International Conference

(1) * Z Wang, J Guo, L Sun, T Kawaguchi, S Hashimoto: On-Line Diagnosis of Heater Wire Breakage, Proceedings of International Conference on Technology and Social Science 2023 (ICTSS 2023), IPS06-04, pp.1-6, (Dec. 2023) (invited)